Positron annihilation in latex templated macroporous silica films: pore size and ortho-positronium escape

L. Liszkay, F. Guillemot, C. Corbel, J.P. Boilot, T. Gacoin, E. Barthel, A. Pérez, M.F. Barthe, P. Desgardin, P. Crivelli, et al.

Positron annihilation in latex templated macroporous silica films: pore size and ortho-positronium escape

L Liszkay[1], F Guillemot[2]‡, C Corbel[3], J-P Boilot[2], T. Gacoin[2], E Barthel[4], P Pérez[1], M-F Barthe[5], P Desgardin[5], P Crivelli[6], U Gendotti[6] and A Rubbia[6]

[1]CEA, Irfu, Centre de Saclay, F-91191 Gif-sur-Yvette, France
[2]Groupe de Chimie du Solide, Laboratoire de Physique de la Matiere Condensée, UMR CNRS 7643, École Polytechnique, 91128 Palaiseau, France
[3]Laboratoire des Solides Irradiés, École Polytechnique, 91128 Palaiseau, France
[4] Surface du Verre et Interfaces (CNRS/Saint-Gobain) UMR 125, 39 quai Lucien Lefranc, 93303 Aubervilliers, France
[5]CNRS, UPR3079 CEMHTI, 3A rue de la Férollerie 45071 Orléans Cedex 2, France
[6]Institute for Particle Physics, ETH Zurich, 8093 Zurich, Switzerland

E-mail: `laszlo.liszkay@cea.fr`

Abstract. Depth profiling of positron annihilation characteristics has been used to investigate the pore size distribution in macroporous PMMA latex templated SiO_2 films deposited on glass or Si and prepared with 11-70% porosity. The correlation between the annihilation characteristics shows that o-Ps escape (re-emission) into vacuum occurs in all films with a porosity threshold that is pore size dependent. For $60 \pm 2\%$ porosity, the o-Ps reemission yield decreases from ~ 0.25 to ~ 0.11 as the pore size increases from 32 to 75 nm. The o-Ps reemission yield is shown to vary linearly with the specific surface area per mass unit and the slope is independent of pore size, 9.1 ± 0.4 g cm^{-1}. For 32 nm pores, the o-Ps annihilation lifetimes in the films, 17(2)ns and 106(5) ns, show that o-Ps annihilates from micropores with small effective size (1.4 ± 4 nm) and from macropores with large effective size (~ 32 nm). Above the porosity threshold, the o-Ps-escape model predicts the annihilation lifetime in the films to be 19 ± 2 ns. Our results imply that o-Ps efficiently detects the microporosity present in the silica walls. At low porosity, its capture into the micropores competes with its capture into the macropores. At higher porosity (when the distance between micropores and macropores become small), this capture into the micropores assists the capture into the macropores.

PACS numbers: 78.70.Bj, 61.43.Gt, 41.75.Fr, 36.10.Dr,

Submitted to: *New J. Phys.*

‡ Present address: Saint Gobain Recherche, 39 quai Lucien Lefranc, 93303 Aubervilliers, France

1. Introduction

Porous silica exists in many different forms with a large variety of pore size and distribution. The pore size can extend from sub-nanometer channels in pure silica zeolites throug mesopores of a few nanometers diameter to macropores of 50-100 nm diameter. As it is known since the early studies of Paulin and Abrosino on silica nanopowders (fumed silica) [1], positron implantation in silica results in an abundant production of positronium (Ps), a bound positron-electron pair, that can escape from silica into vacuum.

Positron and positronium have been extensively used to probe various properties of condensed materials [2, 3, 4, 5]. Ps is formed for 25% in the antiparallel spin singlet state, para-positronium (p-Ps), and for 75% in the spin triplet state, ortho-positronium (o-Ps). In vacuum, Ps self-annihilates with the emission of two gamma photons of ~ 511 keV for the p-Ps state and of three gamma photons with a continuous energy distribution from 0 to 511 keV for the o-Ps state. The lifetimes in the ground state are 125 ps for p-Ps and, about three orders of magnitude longer, 142 ns for o-Ps. In matter, the interaction with electrons modifies the Ps states and reduces their lifetimes. The pick-off process, where annihilation takes place with an electron of the medium converts efficiently spin triplet into spin singlet, which quenches the o-Ps lifetime to lower values than 142 ns and reduces the three gamma annihilation mode. The lifetime depends on the electronic density and can be reduced to values as low as 0.3-1 ns. Vacancy–type defects, such as cavities or pores can capture Ps. This process gives rise to long lifetimes that, for a given material, depend on the pore size and pore surface chemistry. Calculations show that the lifetime increases with the pore size. The comparison between calculated and measured lifetime can be used to determine an effective size for the pores that localize Ps [6, 7, 8, 9, 10, 11].

Various slow positron beam-based spectroscopic methods can be used to investigate Ps annihilation in porous materials. The large variety of pore structures available in porous silica with well controlled pore size and symmetry provides a unique opportunity to study the positronium behaviour in pores. Various authors have reported such studies in mesoporous silica films with approximately 2-8 nm pores. A number of authors have observed that the porosity of the mesoporous silica films affects the re-emission (i. e., escape) of positronium into vacuum [12, 13, 14, 15, 16, 17, 18, 19, 20, 21, 22]. Some of them have systematically investigated Ps escape as a function of porosity and have given evidence of the existence of a porosity threshold for o-Ps escape [23, 24, 21]. Recently, the formation of the Ps_2 molecule [25], the effect of the quantum confinement of Ps [26, 27, 28], Ps-Ps interactions [29, 30] and pore cavity–induced shift of the Ps Lyman-α transition [31] have also been investigated in mesoporous silica films.

To date, there is a lack of study concerning macroporous silica films with pores larger than 10 nm diameter. Such films are of potential interest for optical applications that require coatings with tunable and low refraction index [32, 33]. Compared to nanoporous silica films, macroporous silica films have the advantage to be much less

prone to capillary condensation of atmospheric water. Another applications are the production of positronium target clouds suitable for interaction with antiproton pulses in a next generation of antimatter experiments [34, 35] and improvement in the precision of Ps atomic level spectroscopy measurements [36]. One question is whether macroporous films can reemit o-Ps with efficiency as high as found in mesoporous silica films where o-Ps escape yield can reach more than 40%, depending on the film porosity [20].

In a set of silica films systematically prepared on glass or silicon using PMMA latex spheres (31-75 nm) as sacrificial templates, Guillemot et al [32, 33] have shown that it is possible to control extrinsic porosity for which they determined the following properties. The pore size distribution is sharp and centered at pore size 31, 32, 51 or 75 nm depending on the film [32]. The pores are homogeneously dispersed in the film volume and the distribution is disordered [32]. Furthermore, Guillemot et al performed ellipsometry-porosimetry based on ethanol vapor sorption in the films. For any pore size, the specific surface area per volume unit (σ_v) thus determined exhibits a steep transition as porosity increases at values $> 40 - 55\%$. Below this threshold, σ_v is much lower than expected from the macropore size and associated porosity. Above, σ_v varies quasi linearly and has a value about 1.7 higher than expected on the basis of geometrical model assuming spherical pores.

Similar batches to those in [32] of macroporous PMMA-templated silica films deposited on glass or Si are used here to investigate the depth dependence of positron lifetime spectra and/or 2γ and 3γ annihilation mode fractions. In addition, the effect of 900°C annealing is investigated. For the films prepared with deposition on Si, the characterization of the porosity has been performed before 900°C annealing as described in [32]. However, the ellipsometry based methods described in [32] fail to work in PMMA- template films deposited on glass. The optical contrast between the layer and the substrate is then too low for a reliable application of such methods.

As earlier described for mesoporous silica films [20, 21, 22] a unique lifetime spectrometer in-line on a (1-6 keV) positron beam (IRFU-ETHZ) was used to perform the lifetime measurements for one batch of PMMA- templated 32 nm pore size SiO_2 films deposited on glass. The equipment records o-Ps annihilation decay both inside and outside of the film. The advantage of this equipment is that it allows a unique and reliable determination of the yield for o-Ps escape and annihilation lifetimes of the pores that reemit Ps. Energy spectroscopy of the annihilation gamma is used to determine the fractions of 2γ and/or 3γ annihilation mode in all other PMMA films on Si. The equipment is mounted in-line on a continuous (CEMHTI) slow positron beam. The depth dependence is investigated by varying the positron implantation energy in the range 0.5-15.5 keV.

The present work gives evidence that a porosity threshold for Ps reemission, at $57 < p(\%) < 62$, exists in the 32 nm films deposited on glass or Si. The o-Ps reemission yield is as high as 23(1)% at 62% porosity. Below this threshold, the annihilation lifetimes in the films give evidence that two kinds of pore distribution compete for capturing o-Ps. One type corresponds to micropores with small effective sizes (1.4 ± 0.4

nm). The other one corresponds to macropores with large effective sizes (~ 32 nm). The smaller size is in agreement with the microporosity (< 2 nm) expected in the silica walls on the basis of FTIR measurements in [32] conducted on films deposited on Si. It follows that both the intrinsic microporosity in the silica walls and the extrinsic macroporosity between the silica walls are detected by o-Ps in the 32 nm films deposited on glass. For the larger pore size (51 and 75 nm), it is shown how to correlate the annihilation fractions in the films for the 3γ and 2γ modes to get evidence that o-Ps re-emission is triggered at porosity $52(1) < p(\%) < 56(1)$. Above the o-Ps escape threshold, the 3γ annihilation mode is found to be proportional to the specific surface area of the pore distribution with a constant independent of the pore size.

The paper is organized as follows. After the Introduction in section 1, the experimental details are given in section 2. Section 3 presents the energy dependence of the positron annihilation measurements and their analysis. Section 4 introduces the positron and positronium quantum states that give rise to the annihilation characteristics and discusses their depth dependence. Section 5 examines how the pore size and/or porous volume - determined on ellipsometry based methods in films deposited on Si as in [32]- affects the Ps annihilation characteristics. Finally, section 6 demonstrates that via o-Ps annihilation lifetime and escape, positron annihilation spectroscopy yields novel information on both intrinsic and extrinsic porosity in the PMMA films deposited on glass.

2. Experimental details

Section 2 deals with experimental aspects. This section describes the positron spectroscopic techniques based on positron beam implantation that are used to obtain the data presented in Section 3. The basic properties of positron and positronium physics necessary for the interpretation of the data are introduced in Section 4.

For films on Si substrates (section 2.1), the pore structure is well characterized using ellipsometry related methods as described in [32]. Films on glass are not suitable for such characterization. Section 2.2 describes the energy spectroscopy of the annihilation gamma photons (0-511keV) that is used to investigate how the 2γ and the o-Ps 3γ annihilation mode change with the pore size and porous fraction in the films on Si. Section 2.2 introduces the o-Ps lifetime and reemission spectroscopy used in the present work as an alternative method for investigating the pore size distribution in films on glass. As earlier shown for mesoporous silica films [20, 21, 22], this spectroscopy is a unique tool for investigating o-Ps annihilation decay both inside and outside of the films. It yields information on the size of the pores that capture Ps and, via the o-Ps 3γ annihilation lifetime, on the pore capacity to reemit (or not) Ps into vacuum.

2.1. Macroporous PMMA-templated SiO_2 films: preparation and properties

As described in [32], the porous PMMA latex templated silica films have been prepared by sol-gel method using PMMA latex nanoparticles of 31-32, 51 and 75 nm diameter as sacrificial templates with the porosity (i. e porous fraction in the films) in the range 11-70%. As many as 57 different porous films were measured by positron annihilation among which there were 25, 16 and 16 prepared with 31-32 nm, 51 and 75 nm pore diameter, respectively. The full width at half-maximum of the size distribution of the latex nanoparticles determined by dynamic light scattering (DLS) was less than 10 nm for all the three pore size distributions [32, 33]. The thin films were deposited on silicon or glass surface by spin coating. In the following we use the $SiO_2(d, \Phi)$/substrate designation for a porous film of d (nm) pore size and $\Phi(\%)$ porosity, deposited on a given substrate. From the 31-32 nm films, three sample sets were prepared. The same sol with varying porosity was deposited on silicon or glass in Batch 1 ($SiO_2(32nm, \Phi)$/glass and SiO_2(32 nm,Φ)/Si) while Batch 2 was prepared from a different sol and deposited on silicon (SiO_2(31 nm,Φ)/Si). The templates were removed by heating the films at 450°C in air. In addition, for each pore size, a set of films with varying porosity was heated to 900°C after preparation. The thickness, pore size and porous fraction were determined for each film preparation before 900°C annealing using spectroscopic ellipsometry as described in [32]. As shown for several batches of films prepared in various conditions in [32, 33], the pore size distribution in the films, as experimentally determined on the basis of spectroscopic ellipsometry, and that of the sacrificial latex nanoparticles, as experimentally determined from dynamic light scattering, are the same. Other characterisations such as SEM ellipsometry-porosimetry and FTIR are expected to give similar results in these films as those obtained in [32] since the films are prepared in the same conditions. SEM pictures in [32] show clearly the disordered distribution of the pores. In addition, for 32 and 77 nm pore size, the mean thickness of the silica walls between the pores seen in the SEM pictures significantly decreases with porosity increasing from 0.34 to 0.70(6). Furthermore, the SEM pictures clearly show that for porosity values 0.34(1) and 0.46(2), the mean thickness of the walls increases with pore size. On the basis of spectroscopic ellipsometry [32] and using the density of dense fused silica, 2.2 g cm^{-3} for the SiO_2 silica network in the walls between the extrinsic pores, the porosity in the films varies in the range 0.11-0.71 depending on their preparation. This corresponds to a set of films where the density varies from 0.63-1.95 g cm^{-3} and the refractive index in the range 1.1 to 1.45 [32, 33].

In addition to the extrinsic porosity controlled by tuning the film preparation, there is also an intrinsic microporosity in the sol-gel silica walls that is less easy to control. From the porosity dependence of the refractive index, it seems that the contribution of the microporosity in the PMMA-templated films remains almost constant as more extrinsic porosity is introduced by increasing the fraction of sacrificial PMMA particles in the films. An interesting property of the microporosity in the films is reported in [32]. In contrast with the intrinsic microporosity (pore size < 2 nm), in a CTAB-templated

mesoporous silica (4 nm pore size), the partial pressure dependence of ethanol adsorption isotherms shows that ethanol capillary condensation is absent in the PMMA-templated films. This result suggests that micropores are not detected by this method. It is mentioned in [32] that FTIR experiments performed in films shows that curing the films at increasing temperature up to 450°C results in a progressive decrease of the intensity for the Si-OH stretching band (950 cm^{-1}) and for the hydroxyl stretching band (3000 cm^{-1}). However, there is still a fraction of silanol groups remaining after heating at 450°C, suggesting that a few percent of microporosity subsists in the silica walls.

For some films on Si, annealing is performed at 900°C with 5°C/min heating rate. The 900°C heating is followed by a slow quenching stage where the film/Si samples are directly taken out of the oven and then let cool down at room temperature. The ellipsometric data (thickness, porous fraction) that have been determined for films on Si with big pores (> 50 nm) as well as the morphology of the films as observed using SEM keep constant up to 900°C annealing [33]. After heating at 1000°C, the complete collapse of the porous structure and the oxidation of the silicon substrates are observed.

2.2. Positron annihilation measurements

The SiO_2/glass or SiO_2/Si films were re-heated at 450°C with 1°C/min heating rate a few minutes before mounting in the vacuum chamber of the positron spectrometers. Our earlier studies on mesoporous films have indeed shown that re-heating such porous silica films is necessary for improving the reproducibility of the positron measurements. This is probably due to the removal of water that penetrates in the pores during ageing in ambient atmosphere. The energy distribution of the annihilation γ photons, 0-511 keV, was measured as a function of the positron beam energy in the 0.5-15.5 keV range at the slow positron beam at CEMHTI (Orleans, France [37]), equipped with a high purity, high resolution germanium detector. The 3γ annihilation fraction, i.e. the fraction of e^+-e^- pairs that annihilates emitting three gamma photons, was determined from the relation between the integral for the 511 keV annihilation peak and the integral over an energy range below the peak. The line shape of the 2γ annihilation gamma peak was determined using the low momentum annihilation fraction of the e^+-e^- pairs. It is calculated from the energy spectra as $S_{2\gamma} = A_c/A_{tot}$, where A_c is the integral for a narrow energy region centered at 511 keV, 511 ± 0.656 keV, and A_{tot} is the total integral of the 511 keV annihilation peak. Typically 3×10^6 annihilation events were collected at each positron energy value.

Energy dependent positron lifetime studies in the 1-6 keV energy range were performed at the large acceptance ortho-positronium lifetime spectrometer [21, 38], built in collaboration between IRFU and ETHZ and installed on a slow positron beam of ETHZ [39]. The spectrometer was designed to allow precise determination of positronium lifetime components in the 5-142 ns range in the presence of a significant ortho-positronium escape fraction. Its large detector can register all annihilation events with equal efficiency. Another fundamental problem with the correct measurement of

annihilation spectra where 3γ events are present is that the detection efficiency of the scintillator crystals is different for 3γ and 2γ annihilation signals. We used Monte-Carlo simulation of the detector to optimize the detection threshold of the annihilation photons and avoid distortion of the relative intensities due to this effect [38]. Approximately 3×10^6 events were collected in each lifetime spectra. The lifetime distribution was analysed using the LT program [40].

3. o-Ps lifetime components, three gamma annihilation fraction and low e^--e^+ pair momentum fraction versus positron energy

This section presents first the positron energy (E_{e+}) dependence of the longer components (τ_2, I_2) and (τ_3, I_3) of the lifetime spectra in SiO_2(32 nm)/glass and of the 3γ annihilation fraction ($F_{3\gamma}$) in SiO_2(32 nm)/Si. The sol-gel SiO_2 have been prepared in the same conditions for the films deposited on glass and those deposited on Si. The porosity varies in the range 20-62%.

Then the positron energy dependence of the 3γ annihilation fraction ($F_{3\gamma}$) is illustrated for the three batches of SiO_2(31, 51 or 75 nm)/Si films. The sol-gel SiO_2 films have been prepared in the same conditions for the three batches with porosity varying in the range 11-72% . In addition, the correlation between the three gamma annihilation fraction ($F_{3\gamma}$) and the low e^--e^+ pair momentum fraction ($S_{2\gamma}$) is illustrated for SiO_2(31 nm)/Si.

3.1. o-Ps lifetime components and 3γ annihilation fraction ($F_{3\gamma}$) as a function of positron energy (E_{e+}) in 32 nm pore structure for 20.9-61.6% porosity

o-Ps lifetime components versus E_{e+} (1-6 keV). For each E_{e+} value, the e^+ annihilation lifetime distribution is assumed to be a sum of exponential lifetime decay components. After background corrections and convolution with the 5 ns FWHM resolution function of the spectrometer, the number of the exponential decay components resolved in the fitting of the spectra (see section 2.2) is three in SiO_2(32 nm)/glass over the whole range of porosity, 20.9-61.6%. Given the 5 ns resolution, the shortest component, $\tau_1 < 4$ ns is disregarded due to the possible inaccuracy of its determination. Only the two longer ones, $\tau_{2,3} >\sim 10$ ns are shown in figure 1 (abcd) versus E_{e+}. One notices that the lifetime components for the lower porosity in the range 20.9-48.4% have similar features while the lifetime components for the higher porosity, 61.6%, behave quite differently.

For lower porosity, $\tau_2(E_{e+})$ varies between 9.4 and 20.6 ns with $I_2(E_{e+})$ in the range 5-14%. The lifetimes $\tau_3(E_{e+})$ vary in the range 95 to 117 ns with the intensities $I_3(E_{e+})$ between 2 and 10%. A detailed examination of the curves shows that the porosity slightly affects the dependence of the components with positron energy E_{e+} as follows.

- For $\Phi = 30.6\%$, as E_{e+} increases from 1 to 6 keV, the shorter lifetime, τ_2, decreases. There is a step between 2-3 keV where it remains at the constant value, 15.5(1) ns.

The intensity I_2 has the constant value of 6.6(4)% up to 4 keV and then increases to 14.8(2) at 6 keV. The longer lifetime, τ_3, decreases from 108(1) ns to 98(1) ns between 1-4 keV. Then it stays constant at 95(3) ns. The intensity I_3 decreases continuously from 7.1(2) to 1.9(2)% between 1-6 keV.

- For $\Phi = 38.8\%$, as E_{e+} increases from 1 to 6 keV, the shorter lifetime, τ_2, decreases with a step between 2-3 keV where it remains at the constant value, 15.4(3) ns, whereas the intensity I_2 remains quasi-constant, 5(1)%. The longer lifetime τ_3 remains constant, 103(3) ns, whereas the intensity I_3 decreases continuously from 7.7(1) to 2.0(1)% from 1 to 6 keV.
- For $\Phi = 48.6\%$, as E_{e+} increases from 1 to 6 keV, the shorter lifetime, τ_2, decreases with a step between 3-5 keV where it remains at the constant value, 14.4(2) ns, while the intensity I_2 remains quasi-constant, 7(1)%. The longer lifetime, τ_3, remains constant, 106.8(1.4) ns, whereas the intensity I_3 decreases continuously from 10.1(1) to 2.5(1)% between 1 and 6 keV.

It is worth noting that the lifetime τ_2, for 2-3 keV in SiO_2(32nm,30.6 or 38.8%)/glass and for 3-5 keV SiO_2(32nm,48.6%)/glass, has the same value, 15.2^{+3}_{-8} ns. The lifetime τ_3, for the whole range of E_{e+} has quasi-equal values, 104(4) ns, for 38.8% and 48.6% porosity. For each E_{e+}, τ_3 tends to be lower for the 30.6% porosity than for the higher ones. The difference, however, remains small, 5-10 ns. For 30.6% porosity, τ_3 also tends to decrease and to remain stable only above 4 keV. The lifetime τ_3, for 4-6 keV, has then a value 95(3) ns that is ~ 10 ns lower than that in the higher porosity films.

For the highest porosity 61.6%, the free decomposition for each E_{e+} gives a longer component (τ_3, I_3) well determined ($6 \leq I_3 \leq 22\%$) and found always to decay with a lifetime, $\tau_3 = 142 \pm 2$ ns. This value is characteristic of the o-Ps self-annihilation lifetime in vacuum, $\tau_v = 142$ ns. Accordingly, all lifetime spectra were fitted with τ_3 constant and equal to 142 ns in order to obtain the remaining parameters of the fit, i.e., I_2, I_3, τ_2, with better accuracy. The positron energy dependence of these parameters in figure 1 (abcd) shows that the lifetime τ_2 is nearly constant above 2 keV , 7.8(5) ns. I_2 increases continuously from 4.4(1) to 27.2(1)%. I_3, between 1-2 keV, remains constant, 21(1)%. Then it decreases continuously for $E_{e+} \geq 3$ keV. Its value at 6 keV is 6.3(1)%.

$F_{3\gamma}$ **versus** E_{e+} **(0.5-15.5 keV).** As seen in figure 1 (e), the porosity in the SiO_2(32nm)/Si films affects the positron energy dependence of the three gamma annihilation fraction $F_{3\gamma}$. For any E_{e+} between 0.5 and 4 keV, one notices that $F_{3\gamma}$ systematically increases with porosity, with a peculiarly steep step between 48.4 and 61.6%. $F_{3\gamma}$ for the lower porosity varies in the low range, 0.084-0.01, while the values for the 61.6% porosity vary in the much higher range, 0.2-0.084. For any porosity, $F_{3\gamma}$ reaches 0 for $E_{e+} \geq 10$ keV.

A detailed examination of the $F_{3\gamma}(E_{e+})$ shows that the shape of the curves depend on porosity. The curves $F_{3\gamma}(E_{e+})$ (figure 1 (e)) show similar trends for the lower porosity 20.9-48.4%. $F_{3\gamma}$ decreases quasi continuously as E_{e+} increases. The curves can be decomposed into three parts. The first stage between $0.5- \sim 0.73$ keV corresponds to

a steep decrease. The decrease slows down in the second stage between $\sim 0.73-\sim 4.71$ keV with a slight break at about 1.4-1.5 keV. The decrease slows down further in the third stage between $\sim 4.71-10$ keV. The $F_{3\gamma}(E_{e+})$ curve for the porosity value of 61.6% has a different shape than that for the lower porosity ones. It goes through a maximum between 0.5-1.42 keV and then decreases in two stages, steep between 1.42-5 keV and slow between 5-10 keV.

In summary, as concerns the Ps annihilation characteristics in SiO_2 films on glass or Si, both the Ps lifetime decomposition and the annihilation fraction $F_{3\gamma}$ single out a specific behavior for the higher porosity, 61.6%, when compared to the characteristics at lower porosity $\leq 48.4\%$.

3.2. Three gamma annihilation fraction ($F_{3\gamma}$) versus positron energy (E_{e+}) and versus low e^--e^+ pair momentum fraction ($S_{2\gamma}$).

The three gamma annihilation fraction $F_{3\gamma}$ and the low e^--e^+ pair momentum fraction $S_{2\gamma}$ versus E_{e+} was measured in all the films of the three SiO_2(31, 51 or 75 nm)/Si batches and of the three 900°C annealed SiO_2(31, 51 or 75 nm)/Si batches. The $F_{3\gamma}(E_{e+})$ data are illustrated here for low ($\sim$ 17(6)%), medium ($\sim$ 51(1)%) and high ($\sim$ 65(2)%) porosity only in the as-prepared batches.

In addition, the pore size 31 nm has been chosen to show the typical $F_{3\gamma}(S_{2\gamma})$ curves obtained with E_{e+} as running parameter for low, medium and high porosity.

$F_{3\gamma}$ **versus** E_{e+} **(0.5-15.5 keV).** The annihilation fraction $F_{3\gamma}$ versus E_{e+} measured in SiO_2(31, 51 or 75 nm)/Si at low (17(6)%), medium (51(1)%) and high (65(2)%) porosity can be compared in figure 2 (abc) for the pore diameter values 32, 51 and 75 nm.

One notices that, as the pores size increases from 32 nm to 75nm, the increase between the values $F_{3\gamma}(E_{e+})$ become less and less steep as the porosity increases from low to high in figure 2 (abc). The range of $F_{3\gamma}$ values is 0-0.25 in SiO_2(31nm)/Si (figure 2 (a)), 0-0.17 in SiO_2(51nm)/Si (figure 2 (b)) and 0-0.13 in SiO_2(75nm)/Si (figure 2 (c)). Independently of the size and porosity, one notices that $F_{3\gamma}$ becomes equal to 0 for $E_{e+} \geq 10$ keV.

Porosity affects the shape of the curves in SiO_2(31nm)/Si (figure 2 (a)) as seen above for SiO_2(32nm)/Si (figure 1 (e)). The curve $F_{3\gamma}(E_{e+})$ goes through a maximum at $\sim (0.9-1.42)$ keV for the porosity 66.7% in both films. The maximum value is 0.2535(5) in SiO_2(31nm,66.7%)/Si and 0.210(2) in SiO_2(32nm,66.7%)/Si.

For any value of the porosity in SiO_2(51nm)/Si (figure 2 (b)) and SiO_2(75nm)/Si (figure 2 (c)), $F_{3\gamma}(E_{e+})$ decreases continuously with a slight break at about 1.4-1.5 keV. This break is better marked at medium porosity, 51.2%, SiO_2(51nm)/Si and, medium or high porosity, 50.2 or 63.8%, in SiO_2(75nm)/Si.

$F_{3\gamma}$ **versus** $S_{2\gamma}$ **with** E_{e+} **as running parameter in** SiO_2**(31nm,23.1-66.7%.)/Si.** The annihilation fraction $F_{3\gamma}$ versus low e^--e^+ pair momentum fraction $S_{2\gamma}$ drawn with the positron energy E_{e+} as running parameter can be decomposed in

quasi- linear segments in all the films (figure 3 (abc)). One notices that the number of segments is four (see the insert in figure 3 (a) for 23.1%). The end-points that marked the breaks between the segments correspond to the values ($F_{3\gamma}$,$S_{2\gamma}$) obtained at $E_{e+} \leq 1$ keV, $\sim$ 1.42 keV, $\sim$5 keV and $\geq$ 10 keV, independent of porosity. One notices that the values ($F_{3\gamma}$,$S_{2\gamma}$) are equal to (0,0460(1)) for $E_{e+} \geq 10$ keV.

In summary, these sets of data for the three gamma annihilation mode $F_{3\gamma}$ and the two gamma annihilation mode $S_{2\gamma}$ indicates that the E_{e+} dependence of the annihilation characteristics for both modes are strongly affected both by the pore size and porosity of the pore distribution in the PMMA-templated SiO_2 films.

4. Depth dependence of positron and Ps quantum states

In this section, we examine the Ps annihilation characteristics and the annihilation fingerprints and nature of the Ps annihilation quantum states that give rise to the lifetime components (figure 1), the three gamma annihilation $F_{3\gamma}$ (figures 1, 2 and 3) and the low e^--e^+ pair momentum fraction $S_{2\gamma}$ (figure 3) in the SiO_2/glass or SiO_2/Si films on glass or Si, respectively. For each pore size, the depth dependence is discussed at each porosity value.

4.1. Positron and Ps quantum annihilation states

The positron and Ps annihihation characteristics in SiO_2(porosity)/substrate films results from the superposition of annihilation in various positron and Ps quantum states that can be identified via the positron or Ps annihilation fingerprints in the given state [2]. In addition to p-Ps and pick-off o-Ps annihilation, positron quantum states can also contribute to the $S_{2\gamma}$ values.

The annihilation characteristics measured in the film/substrate in this work are the lifetime $\tau_a(E_{e+})$, the three gamma annihilation fraction $F_{3\gamma}(E_{e+})$ and the low e^--e^+ pair momentum fraction $S_{2\gamma}(E_{e+})$. They are linear combinations of the annihilation fingerprints $(\tau_{a,i}, F_{3\gamma,i}, S_{2\gamma,i})$, weighted by the $f_i(E_{e+})$ annihilation probability from the quantum states i that are accessible to positrons or Ps in the film/substrate.

$$(\tau_a, F_{3\gamma}, S_{2\gamma})(E_{e+}) = \sum f_i(E_{e+})(\tau_{a,i}, F_{3\gamma,i}, S_{2\gamma,i}) \quad (1)$$

The relationship between the lifetime components (I_i, τ_i) in the lifetime τ and the annihilation lifetime, $\tau_{a,i}$, in each state i depends on the processes by which the thermalised positrons at the end of their slow down reach the quantum states from which they annihilate. $F_{3\gamma,i}$ is different from 0 only for triplet annihilation states and is related to $\tau_{a,i}$ by the relationship $F_{3\gamma,i} = \tau_{a,i}/\tau_{o-Psv}v$ where τ_{o-Psv} is the o-Ps lifetime in vacuum, 142 ns. For $1 \leq \tau_a \leq 142$ ns, the $F_{3\gamma,i}$ values vary in the range 0.01-1 and, for $\tau_i \leq 1$ ns, become negligeable, $F_{3\gamma,i} \leq 0.01$.

The annihilation lifetime in film/substrate, $\tau_a(E_{e+})$, is experimentally determined from the lifetime decomposition given in section 3 as

$$\tau_a(E_{e+}) = \sum I_i(E_{e+})\tau_i \quad (2)$$

4.2. Depth Profiling as a function of E_{e+}

For a given energy E_{e+}, the positron distribution as a function of depth z in a film/substrate depends on the positron stopping profile (resulting from slowing down and thermalization) and on the diffusion of the thermalised positrons. In the assumption that the diffusion length is very short, the positron distribution in the film is given by the positron stopping profile. The positron stopping profile for a positron of energy E_{e+} (keV) has been shown to be a Makhovian profie $P(z) = mz^{m-1}/z_0^m exp[-(z/z_0)^m]$, where z is the depth, $z_0 = 0.884\bar{z}$ and the parameter m is 1.8 [43]. The $\bar{z}$ mean penetration depth (nm) of positrons with implantation energy E_{e+} in a material of ρ density is calculated as $\bar{z} = 40/\rho E^{1.6}$ [43]. As the energy E_{e+} increases, the positron distribution gets broader. The probability of annihilation at the film surface decreases while the probability of annihilation in the film bulk contributes more. Above a certain energy, that depends on the film density and thickness, the substrate starts also to contribute.

For the porosity (11-70%) and thickness (200-270 nm) of the PMMA-templated SiO_2 films in this study, the Si substrate starts to contribute for $E_{e+} >\sim 5-10$ keV. For $E_{e+} \geq 10$ keV, the positron distribution reaches 0.98 in the substrate. The annihilation characteristics in the substrate can therefore be determined easily from figures 1, 2 and 3 as $(F_{3\gamma,Si}, S_{2\gamma,Si}) = (0.000(1), 0.458(1))$ for silicon single crystal. Clearly o-Ps is not formed in Si, since $F_{3\gamma}$ is equal to 0.000(1) in agreement with earlier studies [3].

On the contrary, as shown by the lifetime components and the $F_{3\gamma}$ values, the dominant annihilation quantum states in the films ($0.5 < E_{e+} < 5$ keV) are related to o-Ps. To understand the Ps behaviour in the films, it is useful to investigate in details first the films of the 32 nm batch for which the lifetime spectra have been measured and then the other batches.

4.3. Depth dependence of the annihilation states in SiO_2(32,31,55,75 nm)

SiO2(32nm, 61.6%)/glass. For SiO_2(31nm,61.6%)/glass, the existence in the lifetime decay curve of the 142 ns lifetime gives evidence that the film bulk converts a fraction of the positrons implanted in the film bulk into free o-Ps. Depending on the authors, this process is referred as o-Ps reemission or o-Ps escape from the film. This process indicates that Ps annihilation quantum states $|R\rangle$ exist in the film from which o-Ps escapes into vacuum. The reemission (or escape) yield, Y_{Rv}, depends on the annihilation fingerprints in the films τ_R, $F_{3\gamma,R}$ and $S_{2\gamma,R}$ and on the o-Ps escape rate from film to vacuum, κ_{Rv} [21].

The 142 ns lifetime exists in SiO_2(31nm,61.6%)/glass for any E_{e+} in the range 1-6 keV. The intensity decreases above 2 keV (figure 1 (de)), which indicates that the probability for o-Ps escape decreases as positrons get deeper implanted in the film/substrate. In addition to annihilations in vacuum, the existence of the short lifetimes, 8.3 to 7.4 ns with increasing intensity from 1 to 6 keV shows that o-Ps also annihilates in the film.

For each E_{e+} value in the range 1-6 keV, the o-Ps escape model described in [21] is

applied here. From the lifetime decomposition (I_2, τ_2) and $(I_3, \tau_v = 142ns)$ (figure 1 (de)) one calculates the annihilation lifetime, τ_R, the escape rate κ_{Rv}, the annihilation fraction $f_{Rf}(E_{e+})$ for the annihilation lifetime τ_R in the film and $f_{Rv}(E_{e+})$ for the annihilation lifetime 142 ns in vacuum as follows

$$\tau_R = [(\tau_2^{-1} - \tau_v^{-1})I_2/(I_2 + I_3) + \tau_v^{-1}]^{-1} \tag{3}$$

$$\kappa_{Rv} = (\tau_2^{-1} - \tau_v^{-1})I_3/(I_2 + I_3) \tag{4}$$

$$f_{Rf}(E_{e+}) = \tau_R^{-1}(I_2 + I_3)/(\tau_R^{-1} + \kappa_{Rv}) \tag{5}$$

$$f_{Rv}(E_{e+}) = \kappa_{Rv}(I_2 + I_3)/(\tau_R^{-1} + \kappa_{Rv}) \tag{6}$$

Figure 4 (a) shows that the calculated lifetime τ_R varies from 60 ns to 10 ns as E_{e+} increases from 1 to 6 keV. The decrease of τ_R with increasing E_{e+} seems to indicate that the $|R\rangle$ states vary continuously with depth. As seen in figure 4 (a), for $E_{e+} \geq 2$ keV, the calculated curve $\tau_R(E_{e+})$ has the striking property of being similar to the curves $\tau_2(E_{e+})$ experimentally determined in the SiO_2(32nm)/glass films with lower porosity $\leq 38.6\%$. κ_{Rv} decreases from 0.067 to as 0.024 ns^{-1} as E_{e+} increases from 1 to 6 keV.

$F_{3\gamma}$ and $\tau_{a,o-Ps}$ can be calculated for each E_{e+} value as

$$F_{3\gamma} = (I_2 + I_3)(f_{Rf}F_{3\gamma R} + f_{Rv}F_{3\gamma v}), \tag{7}$$

with $F_{3\gamma,R} = \tau_R/\tau_{o-Psv}$, $F_{3\gamma,v} = 1$ (τ_{o-Psv} is the 142 ns o-Ps vacuum lifetime) and

$$\tau_{a,o-Ps} = (I_2 + I_3)(f_{Rf}\tau_R + f_{Rv}\tau_v) \tag{8}$$

For E_{e+} in the range 1-6 keV, the $F_{3\gamma,R}(E_{e+})$ in the film contribute for less than 20 % to $F_{3\gamma}(E_{e+})$. For $E_{e+} = 2$ keV, the reemission yield F_{Rv} at 2 keV is 0.207 nearly equal to the three gamma annihilation fraction $F_{3\gamma}$ at 2 keV, 0.229 (figure 4 (b).

The curve $F_{3\gamma}(E_{e+})$ calculated using the o-Ps escape model is compared in figure 4 (b) to a model curve scaled to the positron stopping profile calculated for the thickness and density of the SiO_2(32nm,61.6%) film. The curve $F_{3\gamma}(E_{e+})$ calculated using the o-Ps escape model seems to decay less than expected from the positron stopping profile in the SiO_2(32nm,61.6%) film.

SiO2(31nm,$\leq$ 48.6%)/glass. For SiO_2(31nm,$\leq$ 48.6%)/glass, the absence in the lifetime decay curves of the 142 ns lifetime indicates that there is no o-Ps escape from the film. The question is whether the two lifetime components in the lifetime spectra can be directly assigned to two types of o-Ps annihilation quantum states in the film that are independently populated. The good agreement between the values $\tau_R(E_{e+})$ calculated above for SiO_2(31nm, 61.6%)/glass with the values $\tau_2(E_{e+})$ for $\Phi \leq 38.8\%$ suggests that one can attribute the lifetime components to two independent kinds of o-Ps states, $|nP\rangle$ and $|mP\rangle$ in the films. The first one, $|nP\rangle$, gives rise to the lifetime values $\tau_{nP}(E_{e+}) = \tau_2(E_{e+})$ and the other one, $|mP\rangle$ to the values $\tau_{mP}(E_{e+}) = \tau_3(E_{e+})$.

For $\Phi < 38.8\%$, τ_{nP} decreases in the range 20.6-9.4 ns as depth gets deeper in the film. For $\Phi = 48.4\%$, τ_{nP} is more stable as a function of depth and the value between 3-5 keV is nearly constant 15.2^{+3}_{-8} ns. The annihilation fraction from these states given

by the intensity $I_2(E_{e+})$ are nearly independent on depth and porosity for $\Phi \leq 48.6\%$ with the value 6(2)% between 2-5 keV.

The values τ_{mP} are quasi-constant 104(4) ns in the whole depth range for 38.8% and 48.6% porosity and tend to decrease as depth increases for $\Phi = 30.6\%$ and to remain lower by 10 ns than for the higher porosity. Fore each E_{e+} value, the value $F_{3\gamma}$ and $\tau_{a,o-Ps}$ are calculated from the lifetime components (τ_2, I_2) and (τ_3, I_3) as

$$F_{3\gamma} \approx I_2 F_{3\gamma,nP} + I_3 F_{3\gamma,mP} \tag{9}$$

with $F_{3\gamma,nP} = \tau_{nP}/\tau_{o-Psv}$ and $F_{3\gamma,mP} = \tau_{mP}/\tau_{o-Psv}$ and

$$\tau_{o-Ps} \approx I_2 \tau_{nP} + I_3 \tau_{mP} \tag{10}$$

SiO_2(31 nm, 20.6-61.6%)/Si, SiO_2(32 nm,23.1-66.7%)/Si. The comparison of the annihilation characteristics between the two different batches of films SiO_2(31 nm, 20.6-61.6%)/Si and SiO_2(32 nm,23.1, 66.7)/Si can be made on the basis of the E_{e+} dependence of the three gamma annihilation fraction $F_{3\gamma}$ in figure 1 (a) and figure 2 (a). The effect of porosity has the same trends in both batches. The $F_{3\gamma}$ annihilation fraction increases with porosity with a steep increase in $F_{3\gamma}(E_{e+})$ between 50 -60 % porosity for any $E_{e+} \leq 10$ keV. One notices however that at lower porosity, $F_{3\gamma}$ is lower in SiO_2(32nm,23.1%)/Si than in SiO_2(31nm, 20.9%)/Si. It shows that the o-Ps quantum states accessible in the films can fluctuate with the film preparation, even for similar pore size and porosity, and have an occupancy or nature that depends on the film preparation.

The correlation between $F_{3\gamma}$ and $S_{2\gamma}$ (figure 3) indicates another interesting property of the annihilation characteristics in the films. As the porosity increases from 23.1 to 61.8%, it becomes easier to distinguish where the depth dependence of the annihilation characteristics reflects a change in the nature or in the occupancy of the annihilations states. The nature of the annihilation states differ at $z > 1$ keV, ~ 1.42 keV, ~ 5 keV and > 10 keV. Between these four mean depths, the linear variation indicates that only the occupancy of the states differs as positrons penetrate deeper in the film/substrate. Independent of porosity, as depth increases in the film from $\sim \bar{z}(1.42keV)$ to $\sim \bar{z}(5keV)$, both $F_{3\gamma}$ and $S_{2\gamma}$ decrease from the values $(F_{3\gamma}, S_{2\gamma})$ at $\sim \bar{z}(1.42keV)$ to $(F_{3\gamma}, S_{2\gamma})$ at mean depth $\sim \bar{z}(5keV)$. Independent of porosity, as the depth increases from $\sim \bar{z}(5keV)$ in the film to the substrate, $F_{3\gamma}$ goes on decreasing while $S_{2\gamma}$ increases to reach the values $(F_{3\gamma,Si}, S_{2\gamma,Si})$ in the Si substrate.

The annihilation characteristics in the films, $(F_{3\gamma}, S_{2\gamma})$ at mean depth $\sim \bar{z}(1.42keV)$, and at $\sim \bar{z}(5keV)$ differ more or less depending on the porosity. However, independent of porosity, $F_{3\gamma}$ and $S_{2\gamma}$ in the films are lower at $\sim \bar{z}(5keV)$ than at $\sim \bar{z}(1.42keV)$. Various annihilation modes contribute to $S_{2\gamma}$: p-Ps, positron and singlet states resulting from o-Ps quenching. The question is whether one of this mode dominates the others and may explain the correlated decrease of $F_{3\gamma}$ and $S_{2\gamma}$ as the mean depth increases in the film. If p-Ps and o-Ps are the only modes, as they are formed for 25% and 75% respectively, $F_{3\gamma}$ and $S_{2\gamma}$ are expected to vary in

a correlated way. One can observe that, for any porosity, the changes in $F_{3\gamma}$ and $S_{2\gamma}$ are uncorrelated. Consequently, other modes contribute, such as positron annihilation and/or o-Ps quenching.

SiO_2(32nm,23.1- 66.7%)/Si, SiO_2(51nm,11.4-65.5%)/Si, SiO_2(75nm,11.2-63.8%)/Si. The strong effect of the size of the pores on the values $F_{3\gamma}(E_{e+})$ in the three different batches of films, SiO_2(32nm,23.1- 66.7%)/Si, SiO_2(51nm,11.4-65.5%)/Si and SiO_2(85nm,11.2-63.8%)/Si (figure 2), indicates that the occupancy or nature of the o-Ps quantum states in the films change when, for a given porosity, the pore size increases.

In summary, to compare the effect of the pore size and porosity on the o-Ps quantum sates, it is safer to choose an energy in the range 1.42-2 keV to minimize the surface effect and maximise the positron distribution in the film as far as possible from the film/substrate interface. The mean positron implantation depth at 1.42 keV positron energy varies in the range 11 to 35 nm for the film density of 0.63-1.95 g cm^{-3}.

5. Pore size and porosity effect on o-Ps annihilation and escape

The annihilation characteristics in the PMMA-templated SiO_2 films have a porosity (Φ) dependence that needs to be examined for each pore size, 31, 32, 51 and 75 nm, to understand how the occupancies and nature of the o-Ps annihilation states in the films, $|nP\rangle$, $|mP\rangle$, $|R\rangle$, and in vacuum $|v\rangle$ are affected by porosity.

5.1. Annihilation lifetimes and fractions at 2 keV in SiO_2(32nm,30.6-61.6%)/glass

Figure 5 (a) illustrates how porosity affects the decay slopes in the lifetime spectra at 2 keV as porosity increases from low (30.6%) to high (61.6%) in SiO_2(32nm)/glass films. On the left of the resolution peak, there are clearly two slopes in the decay curves for the low and high porosity. Both decay slopes change as porosity increases from 30.6 to 61.6%. The fast decay is shorter for 61.6% than for 30.6% whereas the slow decay is longer. The ratio of the number of annihilation events in the slow decay to the fast decay one increases by nearly a factor of ~ 4.6 as porosity increases from 30.6 to 61.6%.

As shown in figure 5 (b), for porosity in the range 30.6-48.4%. the short annihilation lifetimes τ_{nP} at 2 keV have a constant value, 16(1) ns. The annihilation fractions f_{nP} in figure 5 (c) are also constant, 0.06(1). For porosity at 61.6%, the short annihilation lifetimes τ_R at 2 keV has the value 19(2) ns. The annihilation fraction f_R has the value 0.16(1).

The long annihilation lifetimes τ_{mP} at 2 keV (figure 5 (d)) tend to increase, from 102(1) to 109(1) ns with increasing porosity from 30.6 to 48.4%. The annihilation fraction f_{mP} (figure 5 (d)) also increases from 0.06(1) to 0.08(1). For 61.6% porosity o-Ps escape gives rise to the vacuum lifetime 142 ns. The annihilation fraction in vacuum f_{Rv} has the value 0.20 (1).

For the SiO_2(32nm)/glass films, $\tau_{nP}(32nm)$ and $\tau_R(32nm)$, 16-19 ns, are within

15% the same over the whole range of porosity 30.6-61.6%. τ_{nP} and τ_R lifetimes having the same value, it is proposed that the $|nP\rangle$ and $|R\rangle$ states have a similar origin. The threshold for o-Ps escape from the $|nP\rangle$ states is between 48.4-61.6%. From the annihilation fractions f_{nP}, it can be inferred that the occupancy for the $|nP\rangle$ states is rather independent of porosity below 48.4% and increases strongly at 61.6%. It is also proposed that the $|mP\rangle$ states, giving rise to the lifetime $\tau_{mP}(32nm)$, 105(4) ns over the whole range of porosity 30.6-48.4%, have a common origin. From the annihilation fraction f_{mP}, the occupancy for the $|mP\rangle$ states tends to increase with porosity. The occupancy for the v states at porosity of 61.6% is much higher than for the $|mP\rangle$.

5.2. Three versus two gamma mode in SiO_2 porous films at 1.42 keV

This section concerns a detailed analysis of $F_{3\gamma}(S_{2\gamma})$ at 1.42 keV obtained with porosity as running parameter. The analysis is performed for the pore size 31, 32, 51 and 75 nm. It shows that, for a given pore size, the correlation between 3γ and 2γ annihilation mode is strongly dependent on porosity. The pore size affects the porosity dependence of the correlation between 3γ and 2γ annihilation modes.

Independent of pore size, the $F_{3\gamma}(\Phi)$ curve has an S like shape and the $F_{3\gamma}(S_{2\gamma})$ curve has break points where the $F_{3\gamma}$ variation rate with $S_{2\gamma}$ changes from positive to negative as porosity increases. The details are as follows.

- $F_{3\gamma}(\Phi)$ **and** $F_{3\gamma}(S_{2\gamma})$ **at 1.42 keV in SiO_2(32nm,20.9-61.6%.)/Si and SiO_2(31nm,23.1-71.1%.)/Si.** The sol-gel preparation is different for the SiO_2(32nm,20.9.6-61.6%.)/Si and the SiO_2(31nm,23.1-71.1%.)/Si batches. The effect of this preparation difference on the reproducibility of the $F_{3\gamma}(\Phi)$ curve can be examined in figure 6 (a). The $F_{3\gamma}$ values tend to be lower in the second batch, 0.009 instead of 0.03, at porosity $< 40\%$ whereas they are quite comparable for porosity $\geq 45\%$. The curves have very similar S like shapes for the two batches with a well marked step where $F_{3\gamma}$ increases about a factor of 4, from 0.06 to 0.25, while porosity increases by a factor of 1.3 from 48.4 to 66.7%.
  The $F_{3\gamma}(S_{2\gamma})$ curves at 1.42 keV with porosity as running parameter (figure 6 (b)) have three well marked break points. The porosity that corresponds to these break points are 47(1), 57 and 61(1)%. Each break point separates two regions where the rate of variation for $F_{3\gamma}$ versus $S_{2\gamma}$ changes significantly. The break point at 57% is peculiarly interesting because it separates two regions. A transition exists at $\sim 57\%$ where the $F_{3\gamma}$ and $S_{2\gamma}$ variations change from being positively ($< 50.2\%$) to negatively ($\geq 50.2\%$) correlated.
- $F_{3\gamma}(\Phi)$ **and** $F_{3\gamma}(S_{2\gamma})$ **at 1.42 keV for 51 nm pore size in SiO_2(51nm,11.4-65.5%.)/Si.** For 51 nm pore size in SiO_2(51nm,11.4-65.5%.)/Si, the $F_{3\gamma}$ versus porosity (figure 6 (a)) curve has a S like shape with the steep step, 0.057 to 0.113, occurring within 4% of porosity change, between 51-56%. The steep stage separates two regions where $F_{3\gamma}$ increases with porosity at lower rates. The $F_{3\gamma}(S_{2\gamma})$ curves with porosity as running parameter (figure 6 (b)) has a break point at porosity

$\sim 45.5\%$. For porosity $< 45.5\%$, the $F_{3\gamma}$ and $S_{2\gamma}$ variations correlate whereas for porosity $> 45.5\%$ the variations anti-correlate.

- $F_{3\gamma}(\Phi)$ **and** $F_{3\gamma}(S_{2\gamma})$ **at 1.42 keV for 75 nm pore size in SiO_2(75nm,11.2-71.2%)/Si.** For 75nm pore size in SiO_2(75nm,11.2-71.2%)/Si, the $F_{3\gamma}(\Phi)$ curve (figure 6 (a)) has a faint S like shape with the steeper step, 0.0496-0.0861, occurring within 8% of porosity change, between $\sim 50 - 58\%$. The $F_{3\gamma}(S_{2\gamma})$ curve with porosity as running parameter(figure 6 (b)) has a break point at porosity $\sim 50.2\%$. For porosity $< 45.5\%$, the $F_{3\gamma}$ and $S_{2\gamma}$ variations correlate whereas for porosity $> 45.5\%$ the variations anti-correlate.

5.3. Pore size and porosity effect on annihilation states $|nP\rangle$, $|mP\rangle$ and $|R\rangle$

The full set of annihilation characteristics $(\tau, F_{3\gamma}, S_{2\gamma})$ in the PMMA-templated SIO_2 films has been experimentally determined for the 32 nm films whereas only $(F_{3\gamma}, S_{2\gamma})$ data exist in the other 31, 51 and 75 nm films (see section 3). To understand how pore size and porosity affects the annihilation states $|R\rangle$, $|nP\rangle$ and $|mP\rangle$, it is easier to consider first the SiO_2(32nm)/glass and SiO_2(32nm)/Si batches.

For the 32 nm films on glass, the $F_{3\gamma}(\Phi)$ curve is calculated by taking the values calculated at 2 keV (figure 4 (b)) using the lifetime components measured in these films within the framework of the annihilation models described in section 4. The comparison of the calculated and measured curves at 2 or 1.42 keV in the 32 nm films shows that both curves exhibit a steep step in the porosity range 48.4-61.6%. In this range, the annihilation lifetimes give evidence in the 32 nm films on glass that o-Ps escape is triggered. Furthermore, it is in the same porosity range where the variation rate of $F_{3\gamma}$ with $S_{2\gamma}$ from positive becomes negative. The consistency between the porosity values suggests that o-Ps escape also affects $S_{2\gamma}$. $S_{2\gamma}$ is sensitive to the changes in the two gamma annihilation mode and reflects changes in p-Ps and/or e^+ annihilation induced by the triggering of o-Ps escape. As previously reported [41], the triggering of p-Ps escape is also expected at the threshold for o-Ps escape. The p-Ps escape reduces the annihilation fraction from the p-Ps states in the films and, consequently, induces a decrease in $S_{2\gamma}$ at 1-2 keV. In addition, o-Ps escape reduces o-Ps quenching, which also induces a decrease in $S_{2\gamma}$ at 1-2 keV.

The positive to negative transition slope in the variation rate of $F_{3\gamma}$ vs. $S_{2\gamma}$ at 1.42 keV is used in the the 31, 51, 75 nm films measurements to determine the porosity at which of o-Ps escape is triggered. On this basis, the porosity thresholds for o-Ps escape are in the range 57-62%, 51-56%, 52-58% for the 31, 51 and 75 nm pore size films, respectively. The comparison of these thresholds shows that for porosity $\leq 51\%$, o-Ps annihilation takes place only in the films independently on the pore size, 31, 51 or 75 nm. It shows also that o-Ps escape is triggered at porosity $< 57(1)\%$ for the bigger pores, 51 and 75 nm, and above $> 57(1)\%$ for the smaller, 31 nm pores.

For porosity $\leq 47\%$, the $(F_{3\gamma}, S_{2\gamma})$ annihilation characteristics in the films are in excellent agreement for small and medium pores (31, 32, 51 nm). There are slightly

higher for the bigger pores (75 nm). For each pore size, $F_{3\gamma}$ varies quasi-llinearly with $S_{2\gamma}$, which suggests that the 3γ and 2γ annihilation mode reflects mainly Ps annihilation in triplet and singlet states that arises from the same Ps states. As shown in the $F_{3\gamma}$ calculation for the 32 nm SiO_2 films, the states that contribute for 80-90% to $F_{3\gamma}$ are the $|mP\rangle$ states with τ_{mP}, 104(9) ns pores. Another most interesting feature for the films with smaller(32 and 31 nm) pores is that, in addition to the o-Ps escape transition at porosity $> 57\%$, there is a precursor transition at porosity $> 48.4\%$ where the variation rate of $F_{3\gamma}$ with 2γ increases by a factor 2.5. This precursor transition is absent in the 51 or 75 nm films. This precursor transition occurs in a range of porosity where the annihilation fraction for the longer o-Ps lifetime, τ_{mP}, increases (figure 5). This is consistent with the high contribution of o-Ps and p-Ps in these states to $F_{3\gamma}$ and $S_{2\gamma}$, respectively.

5.4. Effect of 900 °C annealing on 3γ annihilation mode at 1.42 keV

The comparison of the $F_{3\gamma}(\Phi)$ curves measured in as-prepared and 900°C annealed SiO_2(31, 51 or 75 nm) films on Si shows that the discussion of the effect of annealing requires to consider the pore size before annealing. The porosity and pore size in figure 7 are determined before 900°C annealing.

The most dramatic changes occur for the small pores (31 nm). The 900°C annealing effect depends on the porosity and can be discussed in considering first a low porosity range $\leq 52.5\%$ and a high porosity range $> 57\%$ separated by a narrow region $\sim 57\%$, where the annealing has a minimum of effect. In the low porosity range, $\leq 52.5\%$, the annealing induces an increase in $F_{3\gamma}$. For porosity $\leq 40\%$, the annealing effects remain weak within the fluctuations for $F_{3\gamma}$ measured in various batches. Between 45-52.5%, the values in 900°C annealed films are 1.5 -2 times higher than the values $F_{3\gamma}$ measured in as-prepared films. In the high porosity range $> 57\%$, the 900°C annealing induces a steep decrease in $F_{3\gamma}$ and the effect is worse with increasing porosity.

For the bigger pores (51 or 75 nm), the trend is systematic as concern the effect of 900°C annealing. Independently on porosity, $F_{3\gamma}$ is higher in the annealed films than in the as-prepared films. The increase tends to be larger with porosity increasing in the range, $\geq\sim 45\%$ and $\geq\sim 55\%$, for 51 nm and 75 nm pores, respectively.

There is a clear effect on the occupancy or nature of the o-Ps annihilation quantum states induced by the 900°C annealing. A process takes place that increases the annihilation probability from states with longer o-Ps annihilation lifetimes. An additional process seems to take place for the 31 nm pores at porosity $\sim 57\%$ that overcomes this process. This second process gives rise to annihilations that produces shorter lifetimes than in annealed films. It overcomes the first process very efficiently as porosity increases.

6. Ps annihilation and escape in intrinsic and extrinsic pores

The nature of positron or Ps quantum states accessible in a material is controlled by the potential fluctuations in the material. Regions with missing atoms, i.e. open volume defects, give rise to lower potential regions where positrons are repelled by the repulsive electrostatic potential between their positive charge and the nuclei of the atom network that forms the material. If the potential fluctuations are deep enough compared to the potential in the atom network, positrons get localised and annihilate at the site of the open-volume defects. This process has been at the basis of positron (or Ps) defect spectroscopy in matter that is used to detect defects from the atomic (i.e. one missing atom or monovacancy) to nanopore scale. The trapping (i.e., capture) to the open-volume defects can be transition-limited, direct (mono, divacancy etc) or precursor state assisted (dislocations, negatively charged defects) or diffusion limited (cavities, surface). The trapping rate is calculated using the Fermi golden rule [2, 42, 3].

6.1. o-Ps lifetimes in nanopores (< 2nm) and in macropores (31-32 nm)

In the case of porous solids, Ps can be captured in pores depending on the pore size and density per unit volume. The quenching models for o-Ps annihilation by electron pick-off in pores indicate that the ranges 9-20 ns for τ_{nP} or τ_R and 95-117 ns for τ_{mP} (figure 1 (d)) are consistent with o-Ps annihilation from localized states in pores. For a given chemistry of the pore surface, the lifetime increases with increasing pore volume depending on the specific pore geometry. According to the rectangular extension of the Tao-Eldrup model (RTE) [11] that uses rectangular pores instead of the spherical ones in the Tao-Eldrup model [6, 7], the length of the cube that describes the pore in the model increases from 1.08, 1.65 and 1.80 nm with increasing lifetime 9, 16 and 19 ns, respectively. The same model gives for 31, 51 and 75 nm pores approximately 122, 130 and 135 ns ortho-positronium lifetime, respectively.

For τ_{mP} measured in the 32 nm pore SiO_2/glass films, 95-117 ns at any depth or 102-111 ns at $\bar{z}$(2 keV), the expected lifetimes are longer by only a factor $\sim 1.0 - 1.3$ indicating that o-Ps capture takes place in pores with effective size close to 32 nm. It is puzzling that the comparison between the calculated o-Ps lifetimes in pores and the experimental τ_{nP}, τ_R lifetimes gives pore sizes much smaller than the extrinsic 32 nm pores. It follows that in addition to the extrinsic 32 nm pores in [32] o-Ps is captured in micropores of small effective sizes (< 2 nm). In earlier studies on CTAB mesoporous films there was a rather good agreement between the measured o-Ps lifetime values and those expected on the basis of the RTE model [11] for the size of the extrinsic pores, $\sim$ 4 nm, determined by ellipsometry porosimetry [21]. These extrinsic pores were also the only pore distribution sampled by o-Ps below the o-Ps escape in these films.

For the 32 nm films on glass, $F_{3\gamma}$ at 2 keV in figure 4 (b) is calculated using the lifetime τ_{nP}, τ_{mP}, 142 ns in vacuum and the corresponding annihilation fractions (section 4). The porosity dependence of $F_{3\gamma}$ calculated at 2 keV for the 32 nm film on glass or measured at 1.42-2 keV in the 31 or 32 nm films on Si is compared in figure 8. The data

are in excellent agreement. This consistency suggests that the nature and occupancy of the $|nP\rangle$, $|R\rangle$ and $|mP\rangle$ annihilation states are quite similar in the 31-32 nm films on glass or Si. However it is difficult to obtain evidence for the existence of the $|nP\rangle$ states from $F_{3\gamma}$. The ratio between the calculated contributions of the $|mP\rangle$ and $|nP\rangle$ states to the $F_{3\gamma}$ values increase with porosity as follows: $\sim$ 5.1, 6.4 and 8 for 30.5%, 38.6% and 48.4% porosity, respectively. This shows that, for $\leq$ 48.4% porosity, the contribution to $F_{3\gamma}$ arises for more than 83% from annihilation from the $|mP\rangle$ states. For 61.6% porosity, $F_{3\gamma}$ arises mostly from annihilation in vacuum.

To get a better insight into the nature of the pore distributions, using, on the one hand, positron annihilation, as in this present work, or, on the other hand, ellipsometry-porosimetry (as in reference [32]), it is useful to examine how porosity affects the correlation between the 3γ annihilation mode, $F_{3\gamma}$ at 1.42 keV, and the experimental specific surface area per volume unit (σ_v) (or per mass unit (σ_v) (from [32]).

For a homogeneous distribution of spherical pores with d diameter and Φ porosity in the SiO_2 films, the calculated σ_v and σ_m are respectively given by $\sigma_v = \alpha\Phi/d$ and $\sigma_m = \sigma_v/\rho(1-\Phi)$, where ρ the SiO_2 density in the walls between the pores that is taken in [32] equal to the density for dense fused silica 2.2 g cm^{-3} and α is a constant value. Using the porosity, pore size and specific surface area experimentally determined for each film as in [32], the σ_v and σ_m expressions are used to calculate the values expected in the film for a homogeneous distribution of spherical pores of pore size and porosity$(d_{exp}(nm), \Phi_{exp}(\%))$.

6.2. Influence of porosity on 3γ annihilation mode, specific surface area per unit volume and specific surface area per unit mass

$F_{3\gamma}$ annihilation fraction at 1.42 keV and σ_v specific surface per unit volume [32] versus porosity Φ. σ_v has been determined versus porosity in [32] from ellipsometry-porosimetry using ethanol vapor in SiO_2(31, 55 and 77 nm)/Si batches prepared in the same or similar conditions as the SiO_2(32 nm)/glass and SiO_2(31, 32, 55 and 77 nm)/Si used in this paper for positron spectroscopy. The comparison of the porosity dependence of $F_{3\gamma}$ at 1.42 keV and σ_v [32] shows a better correlation for the higher, 51-55 and 75-77 nm pore size in figure 7 (bc) than for the lower ones, 31-32 nm in figure 7 (a).

For the small (31-32 nm), intermediate (51 nm) and large (75 nm) pore size, both quantities increases in three stages with a S like shape. The second stage is steeper than the first and third stage. The details vary depending on pore size. For example, for the small pores for which the discrepancy between the two curves is the largest, the porosity threshold for the steep stage is at $>$ 40 % or $>$ 50% for [32] and $>$ 36% for σ_v. The threshold for the third stage is at $\geq$ 66.7(1)%, for [32] while it is at porosity $\geq$ 43(1)%, for σ_v.

Independently on the pore size, one notices a systematic trend for the porosity threshold at which the second, steep, and third stage begins. The thresholds are

systematically shifted to lower porosity for σ_v than for $F_{3\gamma}$. For the steep stage, the porosity shifts between σ_v and $F_{3\gamma}$ are about 5-10%: from 36 to 45% for the small (31-32 nm) pores, 45 to 51% for the medium (51-55 nm) ones and 45 to 50% for the large (75-77 nm) ones. For the third stage, the porosity shifts between σ_v and $F_{3\gamma}$ are about 6-25%: from 42 to 66.7% for the small (31-32 nm) pores, 53 to 56% for the medium (51-55 nm) ones and, 52 to 58% for the large (75-77 nm) ones.

As seen above, the o-Ps quantum states that contribute mainly to $F_{3\gamma}(1.42keV)$ are the $|mP\rangle$ or $|R\rangle$ states, respectively. The threshold for o-Ps escape from the $|R\rangle$ state has been determined (see section 5) to be triggered at porosity in the range 57-62%, 51-56%, 52-58% for the 31, 51 and 75 nm pores, respectively. The porosity threshold of o-Ps escape are well above the steep stage of increase in σ_v: about 21% higher for 31 nm pore size and by 6-7% higher for 51 and 75 nm pore size. Furthermore, such porosity values are well above those for the threshold of the third stage in σ_v for the 31 nm pores. They correspond to them for the 51 and 75 nm pores. In this third stage, one notes also that σ_v evolves quasi-linearly.

The preceeding comparison shows that, independently on the pore size, the o-Ps escape is triggered at porosity where the specific surface area per volume detected by ellipsometry-porosimetry evolves quasi-linearly. The slopes for the different pores sizes (31,55 and 77 nm) have the values (321,31), (172,55), (120,77) (m^2 cm^{-3}, nm). It is worth mentioning that the ratios between the slopes for the different pores sizes are equal to the ratios between the pore diameters although the experimental σ_v values are 1.7 higher than the calculated values for a homogeneous distribution of spherical pores [32].

$F_{3\gamma}$ annihilation fraction at 1.42 keV versus specific surface area per unit volume (σ_v) or mass (σ_m) with porosity as running parameter. In this part, the σ_m value for a given porosity and a given pore size is determined from the σ_v value. This is obtained from the experimental slopes determined, as indicated above, for the third stage in the pore size dependent curves $\sigma_v(\Phi)$ and using the film density calculated as mentioned above.

The correlation between the shapes of the curves, $F_{3\gamma}$ and σ_v as a function of porosity leads to examine the curves $F_{3\gamma}(\sigma_v)$, or shown in figure 9 (a), $F_{3\gamma}(\sigma_m)$ obtained with porosity as running parameter for the 31, 32, 51 or 75 nm pore size in the SiO_2/Si films. In figure 9 (a), as σ_m increases, one notices that $F_{3\gamma}(\sigma_v)$ systematically increases independently on pore size. The detailed examination shows that for 31, 32 and 51 nm pore size, there is a clear transition that separates two ranges of σ_m values where $F_{3\gamma}$ varies linearly as a function of σ_m with different slopes. The transition is wide for 31-32 nm pore size and more steep for 51 nm pore size. It is hardly visible for 75 nm pore size because the slopes are almost the same over the whole range of σ_m values. The transition region for 31-32 nm pore size corresponds to the σ_m values that are calculated for the porosity where the precursor transition takes place. Independent of pore size, the higher range of σ_m corresponds to the values calculated for porosity (57-66.8%) for the 31-32 nm pores and (51-70%) for the 51 and 75 nm pores. These

porosity values are above those for the o-Ps escape threshold. Most interesting is that the $F_{3\gamma}$ increase rate per σ_m unit in the higher σ_m range has a value independent of pore size: $9.1(4) \times 10^{-4} m^2 g^{-1}$. This is illustrated in figure 10 (b) for the porosity $60 \pm 2\%$. Most striking also in figure 10 (b) is how different the $F_{3\gamma}$ annihilation fraction can be for the same porosity but different size pores.

When σ_m is replaced by σ_v, the same types of correlation are found in the values $F_{3\gamma}(\sigma_v)$. However, the lower and higher range of porosity where the linear relationships exist tend to slightly differ. The higher one corresponds to porosity above the o-Ps escape threshold.

6.3. Intrinsic and extrinsic pore distribution in the PMMA-templated SiO_2 films

The macropores in the PMMA-templated SiO_2 films are expected to capture Ps. In addition to this external pore distribution, as mentioned in section 2, there is more elusive evidence in [32] that the silica network between the pores contain an intrinsic microporosity of a few %. To attribute the existence of the $|nP\rangle$ annihilation states to micropores present in the SiO_2 walls appears to be consistent with the microporosity that is assumed to exist from FTIR data in [32]. As mentioned already above, the occupancy and the lifetime $|nP\rangle$ are nearly independent of porosity up to 48.4%. This is consistent with the porosity–independent contribution of the SiO_2 walls to the refractive index in [32]. In addition, as seen in section 6.1, the τ_{nP} values are associated to effective pore size, ≤ 1.80 nm, which is consistent with the micropore size (≤ 2 nm) expected in SiO_2 sol-gel films.

The $|mP\rangle$ annihilation states have annihilation characteristics consistent with those that can be expected from the extrinsic pore distribution. Their occupancy tends to increase with porosity. As seen above, the effective pore sizes estimated from τ_{mP}, 106(4) ns in the SiO_2(32nm)/glass films appears to be however slightly smaller than the expected size. This trend gets more marked as porosity gets lowers.

The $|R\rangle$ annihilation states exist in all films above the porosity threshold for o-Ps escape. For the 61.6% porosity in SiO_2(32nm)/glass, it seems that the intrinsic pore distribution in the walls as well as the extrinsic pore distribution contribute to these states.

The microporous silica network in the PMMA–templated SiO_2 films is the region where positrons slow down and reach thermal energy. One possible mechanisms for positronium formation in insulators is described by the spur reaction model [44]. In this model, conduction electrons created by positron slowing-down can be captured by positrons at the end of their track to form Ps. Once thermalised, the diffusion length of e^+ and Ps before annihilation are expected to be very short, a few $\mathring{A}$, in the PMMA–templated SiO_2 films on the basis of the good agreement between the scaling of the three gamma annihilation fraction $F_{3\gamma}$ dependence with positron energy to that of the positron stopping profile. Diffusion lengths as short as 8(2) nm for positron and 11(2) nm for o-Ps has been reported in vitreous α-SiO_2 [45], about one-two orders of magnitude lower

than in Si defect-free crystals.

In the low range of porosity, $\leq\sim$ 40%, Ps in the PMMA-templated 32 nm SiO_2 films appears to be more sensitive to the intrinsic microporosity than the extrinsic macroporosity. There is a competition for o-Ps capture in the micropores and macropores that favors the micropores up to 40%. At porosity about 50%, the o-Ps occupancy in the macropores (see figure 5 (e)) starts to increase, indicating that the trapping rate from the macropore distribution becomes significantly higher than the trapping rate arising from the intrinsic micropore distribution. As porosity increases further at 61.8%, o-Ps escape appears to arise from the intrinsic micropores. This suggests that the trapping mechanisms in the macropore distribution goes through different stages: from diffusion-limited to transition limited as porosity increases at values $>\sim$ 40% and from direct to precursor assisted as porosity increases further at values $>$ 62%. At low porosity, the distances between the macropores † is too large compared to the Ps diffusion length that is shortened in the SiO_2 walls by capture in the intrinsic micropores. Only a small fraction of Ps formed in thin layer of silica near the macropore surface can successfully escape trapping from the micropores, reach the macropores and get localised there. At intermediate porosity, this process is enhanced due to the higher density of pores per unit volume that increases the specific surface area (per unit volume or mass) that is accessible to Ps formed in the silica walls. At higher porosity, the micropores become so close to the macropores that it seems that the micropores may act as precursor states for trapping into the macropores, leading, accordingly, to o-Ps escape into vacuum. One possibility is that the role of micropores as precursor states to Ps localisation in the macropores affects the lifetime τ_{mP} below the porosity threshold for o-Ps. This precursor assisted trapping into the macropores competes with direct trapping for the Ps fraction formed in the silica walls near the vicinity of a macropore surface. Due to this process, the lifetime τ_{mP} appears to be shorter than expected. This trend increases with lower porosity because the chance for direct capture in the macropores decreases with decreasing porosity.

For porosity above the threshold for o-Ps escape, as mentioned above, the $F_{3\gamma}$ annihilation fraction is dominated by annihilations occurring in vacuum and, thus, gives the value of the o-Ps reemission yield. It follows then from figure 10 (see section 6.2) that the o-Ps reemission yield and the specific surface area par mass unit have the interesting property to show a linear correlation with pore size at a given porosity. As pore size increases from low (32nm) to medium (51nm) and high (75 nm), the o-Ps yield at porosity 60(2)% decreases by a factor $\sim$ 2.3 whereas σ_m decreases by a factor $\sim$ 2.5.

† The atomic packing factor for a close packed structures of hard spheres (fcc or hcp) ordered structure is 0.74 [47]. The characteristic distances in the fcc structure can for example be used to estimate the distribution of the silica wall thickness in the porous films. For a given pore size and a varying porosity Φ, the lattice constant scales as $(0.74/\Phi)^{1/3}$. For a give pore size, the scaling shows that the wall thickness decreases with porosity. For a given porosity, it shows that the wall thickness increases with pore size. For example, for the 51 nm pore size, the minimum distance between the pores varies from 18 to 0 nm in the (110) direction and between 46 to 21.12 nm in the (100) direction from 46 to 21 nm as porosity increases from 0. 3 to 0.74.

This decrease seems to reflect that the probability for o-Ps to reach a pore decreases with the silica wall thickness. For the same porosity, the mean distance between closest pore neighbours scales linearly with the pore size. Consequently, the diffusion path for positrons and/or Ps in the walls to reach the nearest pores increases with pore size and therefore the probability that Ps is captured into the pores decreases.

For porosity above the threshold for o-Ps escape, as mentioned above, the $F_{3\gamma}$ annihilation fraction is dominated by annihilations occuring in vacuum and, thus, gives the value of the o-Ps reemission yield. It follows then from figure 10 (see chapter 6.2) that the o-Ps reemission yield and the specific surface area per mass unit have the interesting property to show a linear correlation with pore size at a given porosity. As pore size increases from low (32 nm) to medium (51 nm) and high (75 nm), the o-Ps yield at porosity 60(2)% decreases by a factor ~ 2.3 whereas σ_m decreases by a factor ~ 2.5. This decrease seems to reflect that the probability for o-Ps to reach a pore decreases with the silica wall thickness. For the same porosity, the mean distance between closest pore neighbours scales linearly with the pore size. Consequently, the diffusion path for positrons and/or Ps in the walls to reach the nearest pores increases with pore size and therefore the probability that Ps is captured in the pores decreases.

The effect of the annealing at 900°C on the porosity dependence of $F_{3\gamma}$ yields mainly information on the macropore distribution. This can be quantitatively estimated in the the 32 nm SiO_2 films. Using the lifetime and occupancy of the $|nP\rangle$, $|mP\rangle$ and $|R\rangle$ and o-Ps vacuum states, it can be calculated that the contribution of the macropores or vacuum to $F_{3\gamma}$ is about 80-90% before annealing. Except for porosity $> 52\%$ for the 31 nm pores, 900°C annealing tends to increase the $F_{3\gamma}$ fraction in the macropores that localize Ps. Various evolutions of the macropore distribution can result in such increase: increase of pore density, pore size or reduction of o-Ps quenching induced by change in the pore surface chemistry. FTIR gives evidence (section 2.1) that 900°C annealing affects the surface chemistry of the pore. The density of hydroxyl groups (Si-OH) on the pore surface decreases and the groups are replaced by siloxane bonds (Si-O-Si). Otherwise, information on the extrinsic pore evolution based on ellipsometry is lacking. The change in $F_{3\gamma}$ seems most likely to reflect the change in the pore surface chemistry rather than changes in pore density or size. However, for the 31 nm pores, as porosity increases above 52%, the strong decrease of $F_{3\gamma}$ suggests that macropores disappear as porosity increases. To more precisely discriminate which is the dominant process occurring during the 900°C annealing , it is necessary to conduct measurements using o-Ps lifetime and reemission spectroscopy.

7. Conclusion

The present work investigates depth profile of positron annihilation characteristics in PMMA–templated SiO_2 films deposited on glass or Si. According to [32], this extrinsic porosity in the films deposited on Si has a sharp pore size distribution centered at pore size 31, 32, 51 or 75 nm depending on the film. The pores are homogeneously dispersed

in the film volume and the distribution is disordered. Depth profiling is performed by varying the positron implantation energy of slow e^+ beams in the range 0.5-15.5 keV. For the density range of the films determined by spectroscopic ellipsometry in the films deposited on Si [32], 0.63-1.95 g cm^{-3}, the mean depth of implanted positrons varies from 11-35 nm at 1.42 keV to 82-253 nm at 10 keV.

Two types of e^+ annihilation spectroscopy in line with slow e^+ beams are coupled to give a complete picture of Ps annihilation and o-Ps re-emission (i.e. escape) from the films. The o-Ps re–emission into vacuum outside the films on glass is measured in reflection mode with a specially designed lifetime spectrometer installed on the ETHZ beam. Using the lifetime components, it is possible to select the appropriate e^+ energy range in which to determine the fingerprints of Ps annihilation and o-Ps re–emission yield from the film bulk. It is shown that there is a porosity threshold for Ps reemission, at $57 < \Phi(\%) < 62$ for 32 nm SiO_2 films on glass. The o-Ps reemission yield is as high as 23(1)% in these films. Its decrease with film depth seems to match the positron stopping profile. This suggests that the film is homogeneous with respect to o-Ps reemission for depths well beyond the near film surface region.

Using the correlation between 3γ and 2γ annihilation modes (CEMHTI), it is possible to select the appropriate e^+ energy range (typically 1.5 keV to 5 keV) in which to determine the fingerprints of Ps annihilation and o-Ps re-emission yield from the film bulk. The comparison of the porosity dependence of the correlation between the 3γ and 2γ annihilation modes (CEMHTI) with one of the lifetime components (ETHZ) shows that, at the porosity threshold for o-Ps re-emission, the correlation $(F_{3\gamma}, S_{2\gamma})$ changes its direction. Instead of increasing with $F_{3\gamma}$, the contribution from the 2γ annihilation mode, $S_{2\gamma}$, starts to decrease as o-Ps escape from the film into vacuum is triggered.

This specific feature is used in the other films to determine the o-Ps escape from the annihilation characteristics $(F_{3\gamma}, S_{2\gamma})$ at 1.42 keV. This method gives evidence that o-Ps re-emission is triggered at porosity $52(1) < p(\%) < 56(1)$ for 51 and 75 nm pores. The o-Ps escape yield is then approximately equal to the 3γ annihilation fraction $F_{3\gamma}$. Independently on the pore size, the yield is found to be proportional to the specific surface area per unit of mass (or volume). The rate constant is 9.1 ± 0.4 g cm^{-1}.

Below the porosity threshold for o-Ps reemission, the annihilation lifetimes in the 32 nm SiO_2/glass films give evidence that two kinds of pore distribution compete for capturing o-Ps once it is formed in the silica walls. One distribution seems rather independent of porosity and corresponds to small effective pore sizes, 1.0-1.8 nm. In the other, the capture increases with porosity and corresponds to an effective pore size close to the extrinsic pore size, 32 nm. Above the porosity threshold, the o-Ps escape model [21] is used to determine the annihilation lifetime in the pores from which o-Ps are reemitted. The calculations show that their effective size is comparable to the small sizes detected below the o-Ps escape threshold.

It is concluded that o-Ps detects both the intrinsic microporosity in the silica walls and also the extrinsic macroporosity between the silica walls. At low porosity, the intrinsic micropores capture with sufficient efficiency to overcome the contribution from

capture in the macropores. As porosity increases, the number of micropores that get located near the surface of macropores increases. As the distance between them becomes comparable (or lower) than the o-Ps diffusion length in the silica walls, the capture into the macropores becomes assisted by the micropores. This process is triggered when the porosity is high enough for the extrinsic macropores to be open to the vacuum, leading, accordingly, to o-Ps escape.

After removal of the hydroxyl groups from the internal pore surfaces by heating at 900°C, o-Ps capture at the macropores is still observed for the higher pore size, 51 and 75 nm but disappears progressively as porosity increases at values $50 < p(\%) \leq 55$ for the smaller pore size 31 nm.

Acknowledgments

F. G. gratefully acknowledges Saint-Gobain for financial support. This work was supported in part by the SNSF under the Ambizione grant PZ00P2-132059.

Appendix A. Calibration

The 3γ annihilation fraction ($F_{3\gamma}$) is determined from the energy distribution of the annihilation photons by a method that is similar to the procedure applied in [43, 46]. The first step is to experimentally determine the $P(F_{3\gamma})$ net area of the 511 keV 2γ annihilation peak, after background correction. Let's remark that, as the energy distribution of gamma photons from 3γ annihilation events is a continuous distribution between 0 and 511 keV and the width of the detected annihilation peak is small, the contribution of these events to the net area of the peak is negligible.

$P(F_{3\gamma})$ can be expressed as a function of the number of counts for all annihilation events (free positron-electron, para-positronium and ortho-positronium annihilation), N, as follows:

$$P(F_{3\gamma}) = N(1 - F_{3\gamma})g_p, \tag{A.1}$$

where g_p is the probability that a 2γ annihilation event is detected by the spectrometer in the 511 keV peak area. As long as the beam current and the geometry remain identical (i.e., N is constant), it is possible to determine the 3γ annihilation fraction value, $f_{3\gamma}$, in a porous material by measuring a calibration material for which evidence exists from lifetime data that the $F_{3\gamma}$ value is zero. In the case of porous film grown on silicon, the energy distribution of the annihilation gamma photons for Si substrate satisfies this condition. By eliminating g_p in (A.1) one obtains

$$f_{3\gamma} = 1 - P(f_{3\gamma})/P(0) \tag{A.2}$$

When N varies due to drift in the beam conditions, it is necessary to determine $F_{3\gamma}$ using a more sophisticated approach, as in [43, 46]. In addition to $P(F_{3\gamma})$, one also

experimentally determine $T(F_{3\gamma})$, the total area of the annihilation gamma spectrum that starts above the noise level and includes the 511 keV peak:

$$T(F_{3\gamma}) = N(1 - F_{3\gamma})h_p + NF_{3\gamma}h_o \tag{A.3}$$

where h_p and h_o are the probabilities that 2γ and 3γ annihilation events, respectively, are detected by the spectrometer in the total area. The positronium $R_{Ps}(F_{3\gamma})$ parameter [43, 46], which is independent of the beam intensity, can then be determined as

$$R_{Ps}(F_{3\gamma}) = \frac{T(F_{3\gamma}) - P(F_{3\gamma})}{P(F_{3\gamma})}. \tag{A.4}$$

By substituting $F_{3\gamma} = 0$ and $F_{3\gamma} = 1$ into (A.1) and (A.3) we can determine that $Ng_p = P(0)$, $Nh_p = T(0)$ and $Nh_o = T(1)$. By replacing Ng_p, Nh_p) and Nh_o by $P(0)$, $T(0)$ and $T(1)$, respectively, in (A.1) and (A.3) and solving (A.1), (A.3) and (A.4) for $F_{3\gamma}$, we get

$$F_{3\gamma} = \left(1 + \frac{T(1)}{P(0)} \frac{1}{(R(F_{3\gamma}) - R(0)}\right)^{-1} \tag{A.5}$$

The calibration of the ratio $T(1)/P(0)$ is based on the measurements of R_{Ps} in two materials for which $F_{3\gamma}$ is known. For one material, the $F_{3\gamma}$ is known to be 0 and for the other one, the $F_{3\gamma}$ is known to be $f_{3\gamma}$, determined either according to (A.2) or by other means (e.g., from lifetime measurement). The calibration factor $T(1)/P(0)$ is determined by solving (A.5) using the experimental values $f_{3\gamma}$, $R_{Ps}(f_{3\gamma})$ and $R_{Ps}(0)$. Once the calibration is made, the $F_{3\gamma}$ in any material can be calculated by substituting the experimental R_{Ps} into (A.5).

Both R_{ps} and the calibration factor $T(1)/P(0)$ are independent of the positron beam intensity. This intensity may change with positron energy due to positron backscattering and other reasons. The use of a method that is independent of this quantity is essential for the correct determination of the $F_{3\gamma}$ annihilation fraction. For mesoporous silica films deposited on glass, $F_{3\gamma}$ has been independently determined in the same film both from the energy distribution of the annihilation gamma photons using R_{Ps} and from lifetime spectra. An excellent agreement was found between the two methods [20].

References

[1] Paulin R, Ambrosino G 1968 *Journal de Physique* **29** 263

[2] Dupasquier A 1983, in: Proceedings of the International School of Physics Enrico Fermi, Course LXXXIII. Ed. W. Brandt, A. Dupasquier. North-Holland Publishing Company, Amsterdam, New York, Oxford, p510

[3] Krause-Rehberg R, Leipner H S, Positron Annihilation in Semiconductors, Springer Series in Solid State Sciences, Springer, Berlin, 1999

[4] Positron Beams and Their Applications, edited by Paul Coleman, World Scientific, Singapore, 2000

[5] Principles and Applications of Positron and Positronium Chemistry, edited by YC Jean, PE Mallon and DM Schrader, World Scientific, Singapore, 2003

[6] Tao S J 1972 *J. Chem. Phys* **56** 5499

[7] Eldrup M, Lightbody D and Sherwood J N 1981 *Chem. Phys* **63** 51

[8] Goworek T, Ciesielski K, Jasinska B and Wawryszczuk J 1997 *Chem. Phys. Letters* **272** 91

[9] Goworek T, Ciesielski K, Jasinska B and Wawryszczuk J 1998 *Chem. Phys.* **230** 305

[10] Ito K, Nakanishi H and Ujihira Y 1999 *J. Phys. Chem. B* **103** 4555

[11] Dull T L, Frieze W E, Gidley D W, Sun J N and Yee A F 2001 *J. Phys. Chem. B* **105** 4657

[12] Gidley D W, Frieze W E, Dull T L, Yee A F, Ryan E T and Ho H-M 1999 *Phys. Rev. B* **60** R5157

[13] Gidley D W, Peng H G and Vallery R S 2006 *Ann. Rev. Mat. Sci.* **36** 49

[14] Petkov M P, Weber M H, Lynn K G and Rodbell K P 2001 *Appl. Phys. Lett* **79** 3884

[15] Wang C L, Weber M H, Lynn K G and Rodbell K P 2002 *Appl. Phys. Lett.* **81** 4413

[16] Petkov M P, Wang C L, Weber M H, Lynn K G and Rodbell K P 2003 *J. Phys. Chem B* **107** 2725

[17] van Veen A, Escobar Galindo R, Schut H, Eijt W W H, Falub C V, Balkenende A R and de Theije F K 2003 *Mater. Sci. Eng. B* **102** 2

[18] Yu R S, Ito K, Hirata K, Zheng W and Kobayashi Y 2003 *J. Appl. Phys.* **93** 3340

[19] He C, Suzuki R, Ohdaira T, Oshima N, Kinomura A, Muramatsu M, Kobayashi Y 2007 *Chemical Physics* **331** 213

[20] Liszkay L, Corbel C, Perez P, Desgardin P, Barthe M-F, Ohdaira T, Suzuki R, Crivelli P, Gendotti U, Rubbia A, Etienne M and Walcarius A 2008 *Appl. Phys. Lett.* bf 92 063114

[21] Liszkay L, Corbel C, Raboin L, Boilot J-P, Perez P, Brunet-Bruneau A, Crivelli P, Gendotti U, Rubbia A, Ohdaira T and Suzuki R, 2009 *Appl. Phys. Lett.* **95** 124103

[22] Liszkay L 2010 *Physics With many Positrons, Proceedings of the International School of Physics "Enrico Fermi", course CLXXIV*, edited by A. Dupasquier, A. P. Mills, Jr., R. S. Brusa (IOS Press, Amsterdam, Oxford, Tokyo, Washington DC) p 297

[23] Petkov MP, Weber MH, Lynn KG and Rodbell KP 2000 *Appl. Phys. Lett.* **77** 2470

[24] Sun JN, Gidley DW, Hu YF, Frieze WE and Yang S 2002.*Mater. Res. Soc. Symp. Proc.* **726** Q 10.5

[25] Cassidy D B, Mills A P Jr 2007 *Nature* **449** 195

[26] Mariazzi S, Salemi A, Brusa R S 2008 *Phys. Rev. B* **78** 085428

[27] Crivelli P, Gendotti U, Rubbia A, Liszkay L, Perez P and Corbel 2010 *Physical Review A* **81** 052703

[28] Cassidy D B, Crivelli P, Hisakado T H, Liszkay L, Meligne L E, Perez P, Tom H W K and Mills A.P, Jr. 2010 *Phys. Rev. A* **81** 012715

[29] Cassidy D B and Mills A P, Jr 2008 *Phys. Rev. Lett.* **100** 013401

[30] Cassidy D B and Mills A P Jr. 2011 *Phys. Rev. Lett.* **107** 213401

[31] Cassidy D B, Bromley M W J, Cota L C, Hisakado T H, Tom H W K, and Mills A P Jr. 2011 *Phys. Rev. Lett* **106** 023401

[32] Guillemot F, Brunet-Bruneau A, Bourgeat-Lami E, Gacoin T, Barthel E and Boilot J-P 2010 *Chem. Mater* **22** 2822

[33] Guillemot F, thesis, Ecole Polytechnique, Palaiseau, France

[34] Perez P and Rosowsky A 2005 *Nuclear Instrum. Meth. A* **545** 20

[35] A. Kellerbauer et al 2008 *Nucl. Instrum. Meth. B* **266** 351
[36] Crivelli P, Cesar C L, Gendotti U 2011 *Can. J. Phys.* **89** 29
[37] Desgardin P, Liszkay L, Barthe M-F, Henry L, Briaud J, Saillard M, Lepolotec L, Corbel C, Blondiaux G, Colder A, Marie P, Levalois M 2001 *Mat. Sci. Forum* **363-365** 523
[38] Crivelli P, Gendotti U, Rubbia A, Liszkay L and Perez P 2009 *Materials Science Forum* **607** 251
[39] Alberola N, Anthonioz T, Badertscher A, Bas C, Belov A S, Crivelli P, Gninenko S N, Golubev N A, Kirsanov M M, Rubbia A and Sillou D 2006 *Nuclear Instr. Meth. A* **560** 224
[40] Kansy J 1996 *Nucl. Instrum. Methods Phys. Res. A* **374** 235
[41] Eijt S W H, van Veen A, C.V. Falub C V, Escobar Galindo R, Schut H, Mijnarends P E,de Theije F K, Balkenende A R 2003 *Radiation Physics and Chemistry* **68** 357
[42] Puska M, Corbel C and Nieminen R 1990 *Phys. Rev. B* **41** 9980
[43] Schultz P J and Lynn K G 1988 *Rev. Mod. Phys* **60** 701
[44] Mogensen O E 1974 *J. Chem. Phys* **60** 998
[45] Van Petegem S, Dauwe C, Van Hoecke T, De Baerdemaeker J and Segers D 2004 *Physical Review B* **70** 115410
[46] Marder S, Wu C S and Bennett W 1956 *Phys. Rev.* **103** 1258
[47] Ashcroft N W and Mermin N D, Solid State Physics, (Holt, Rinehart, and Winston, New York, 1976)

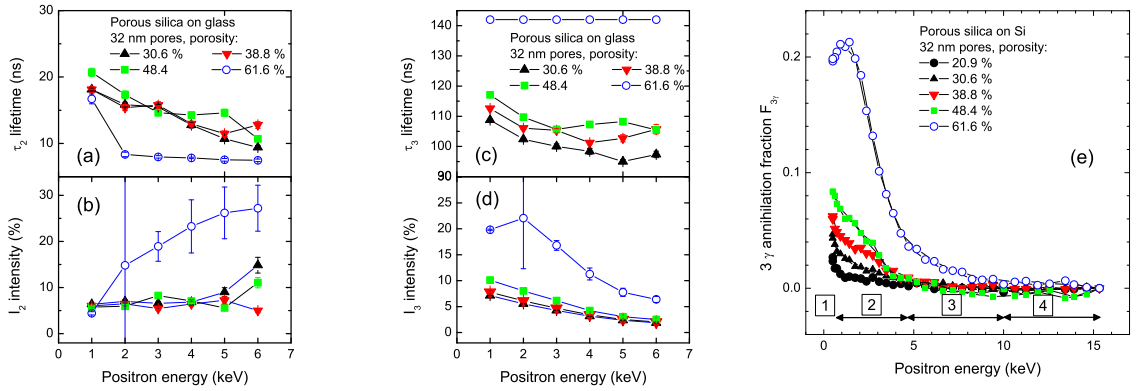

Figure 1. Positron energy dependence of the positron lifetime components (τ_2 (a), I_2 (b)) and (τ_3 (c), I_3 (d)) and of the 3γ annihilation fraction, $F_{3\gamma}$, for low, intermediate and high porosity in (a) 32 nm pore size silica films deposited on glass (abcd) or Si (e). The lines in (e) are calculated $F_{3\gamma}(E_{e+})$ curves using a depth dependent positron distribution based on positron stopping profile in the films and using $F_{3\gamma}$ at 1.42 keV positron beam energy as characteristic value for the films at any depth. $F_{3\gamma}$ in Si is equal to 0.

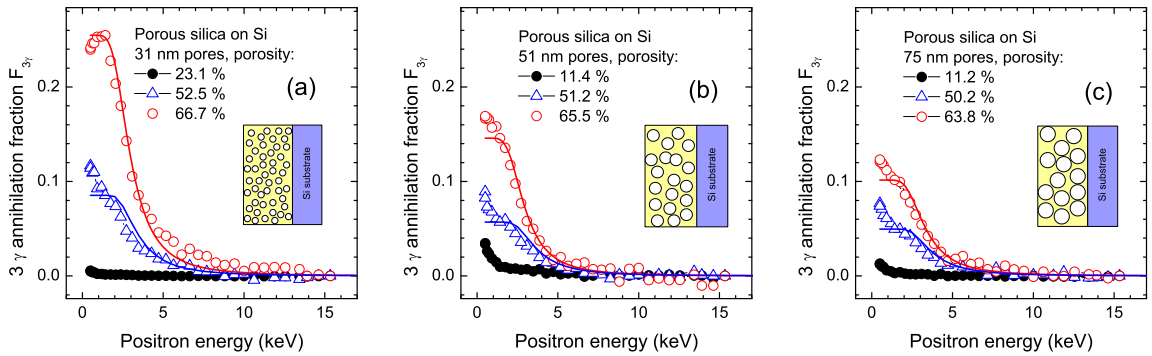

Figure 2. Positron energy dependence of the 3γ annihilation fraction, $F_{3\gamma}$, at low, intermediate and high porosity in (a) 31, (b) 51 and (c) 75 nm pore size silica films deposited on Si. The inserts illustrate the scales between pore size and typical film thickness (255(15) nm). The lines are calculated $F_{3\gamma}(E_{e+})$ curves using a depth dependent positron distribution based on positron stopping profile in the films and using $F_{3\gamma}$ at 1.42 keV positron beam energy as characteristic value for the films at any depth. $F_{3\gamma}$ in Si is equal to 0.

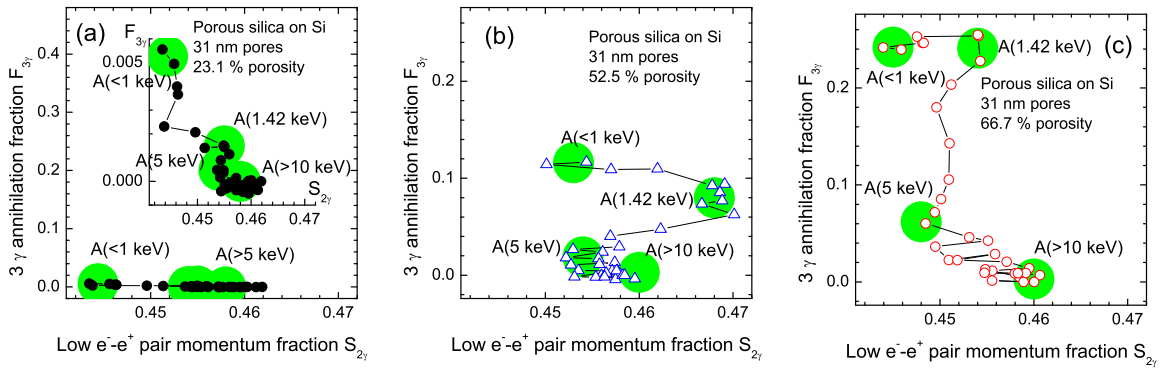

Figure 3. 3γ annihilation fraction $F_{3\gamma}$ versus low e^--e^+ pair momentum annihilation parameter $S_{2\gamma}$ with positron beam energy as running parameter in (a) 31, (b) 51 and (c) 75 nm pore size silica films deposited on Si. The $A(E_{e+})$ points give the positron energy (E_{e+}) values in keV where a transition occurs in the variation of the $F_{3\gamma}(S_{2\gamma})$ curves. The insert in (a) represents the same data plotted on an enlarged scale.

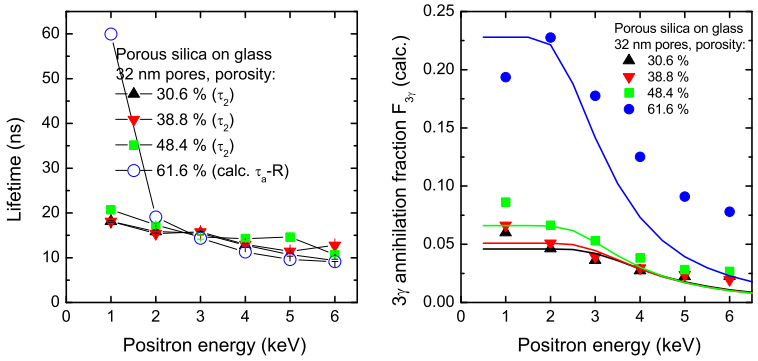

Figure 4. (a) Positron energy dependence of lifetime τ_2 for 30.5, 38.8 and 48.4% porosity and calculated annihilation lifetime, τ_a, from o-Ps escape annihilation state ($|R\rangle$) model for 61.6% porosity in 32 nm pore size silica films deposited on glass. (b) Positron energy dependence of the 3γ annihilation fraction $F_{3\gamma}$, calculated from the independent o-Ps annihilation states ($|nP\rangle$ and $|mP\rangle$) model for 30.5 -48.4% porosity and the o-Ps escape annihilation state ($|R\rangle$ model for 61.6% porosity. The lines are calculated $F_{3\gamma}(E_{e+})$ curves using a depth dependent positron distribution based on positron stopping profile in the films and using the $F_{3\gamma}$ value at 1.42 keV positron energy as characteristic value for the films at any depth. $F_{3\gamma}$ in Si is equal to 0.

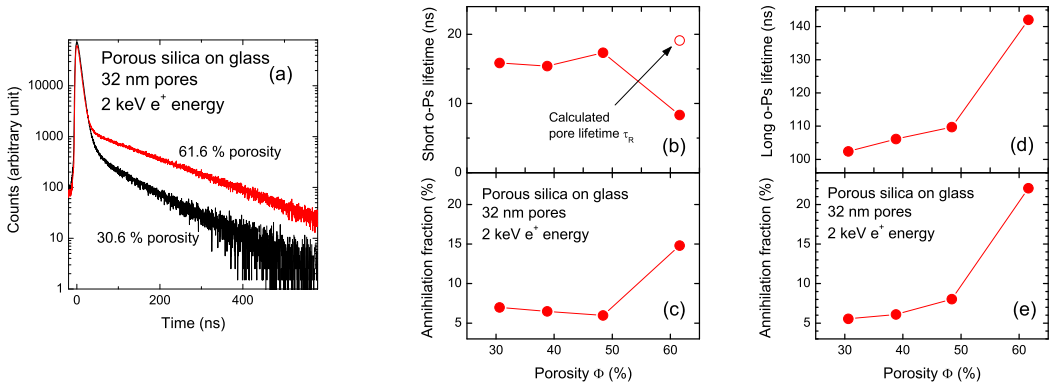

Figure 5. (a) Positron lifetime spectra measured at 2 keV positron energy in 32 nm silica films deposited on glass for 30.5% (lower curve) and 61.8% (upper curve) porosity. Porosity dependence of the (b) short o-Ps lifetimes τ_{nP} and τ_R (the pore lifetime calculated from the o-Ps escape model is given at 60% porosity), (d) long o-Ps lifetimes τ_{mP} and (c,e) corresponding annihilation fraction in macroporous 32 nm pore size silica films deposited on glass. The lifetimes and the annihilation fractions are calculated either from the independent o-Ps annihilation states ($|nP\rangle$ and $|mP\rangle$) model for 30.5, 38.8 and 48.4% porosity or from the o-Ps escape annihilation state ($|R\rangle$) model for 61.8% porosity.

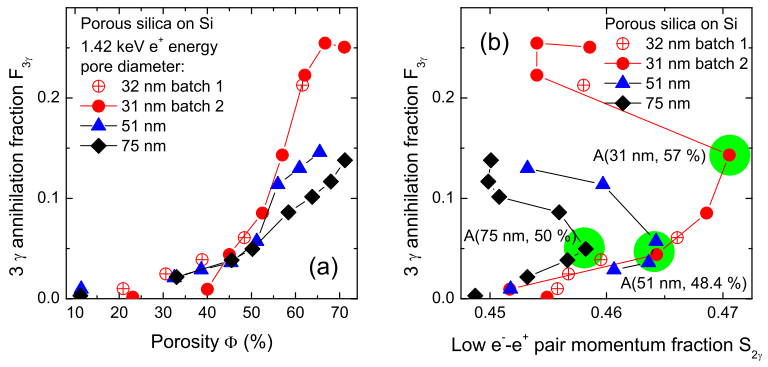

Figure 6. 3γ annihilation fraction $F_{3\gamma}$ at 1.42 keV positron energy (a) versus porosity and (b) versus low e^--e^+ pair momentum annihilation parameter $S_{2\gamma}$ at 1.42 keV positron energy with porosity as running parameter in 31, 51 and 75 nm films deposited on Si. For a given pore size, d_o (nm), the $A(d_o(nm), p(\%))$ points give the value of the porosity where a transition occurs in the variation of the $F_{3\gamma}(S_{2\gamma})$ curves.

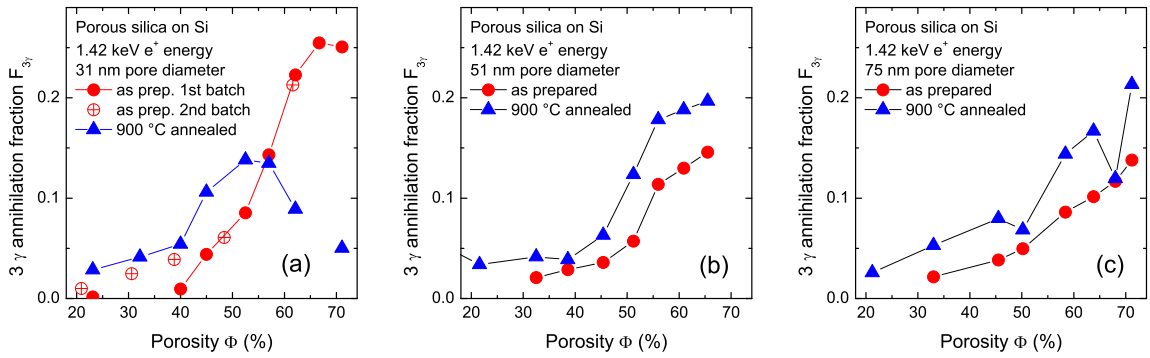

Figure 7. Porosity dependence of measured and calculated 3γ annihilation fraction $F_{3\gamma}$ at 1.42 keV positron beam energy in (a) 31 nm, (b) 51 nm and (c) 75 nm pore size silica films deposited on Si, as-prepared (circles) and annealed at 900°C in air (triangles).

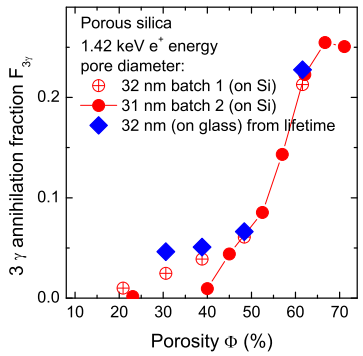

Figure 8. Porosity dependence of measured and calculated 3γ annihilation fraction $F_{3\gamma}$ at 1.42 keV positron energy in 31 nm pore size silica films deposited on Si. $F_{3\gamma}$ is calculated in the independent annihilation model ($|nP\rangle$, $|mP\rangle$) for porosity $\geq$57% and in the o-Ps escape annihilation state ($|R\rangle$) model above the porosity threshold for o-Ps escape, >57%.

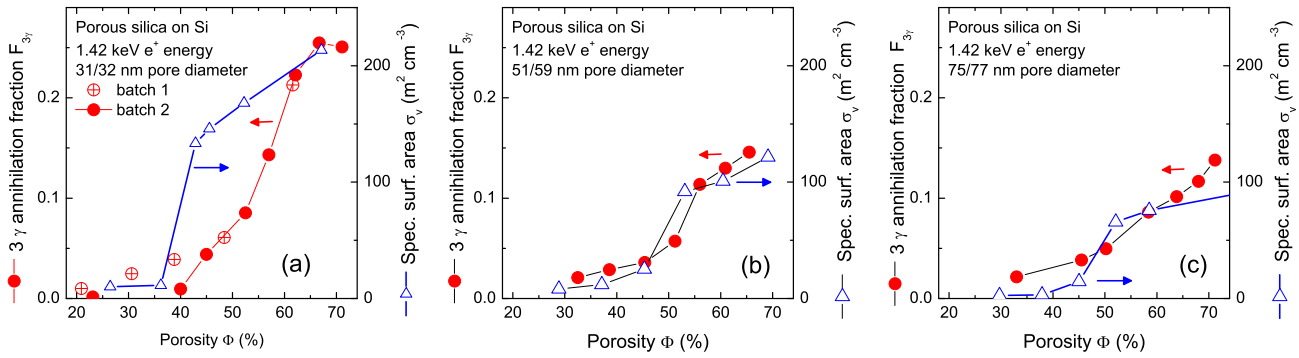

Figure 9. Porosity dependence of 3γ annihilation fraction $F_{3\gamma}$ at 1.42 keV positron energy (right scale) and specific surface area per volume unit (σ_v) form [32] (left scale) in (a) 31-32 nm, (b) 51-59 nm and (c) 75-77 nm pore size silica films deposited on Si.

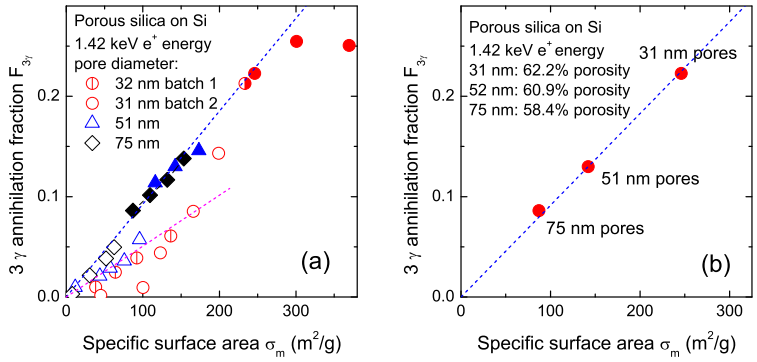

Figure 10. (a) 3γ annihilation fraction $F_{3\gamma}$ at 1.42 keV positron energy as a function of the specific surface area (σ_m) in 31, 51 and 75 nm pore size silica films deposited on Si. The values measured above the porosity threshold for o-Ps escape are plotted with solid symbols. (b) Three gamma annihilation fraction $F_{3\gamma}$ at 1.42 keV for 60(2) % porosity versus σ_m in 31, 51 and 75 nm films on Si.